RESEARCH ARTICLE

Intraseasonal synchronization of extreme rainfall between North India and the Sahel

Felix M. Strnad[1,2] | **Kieran M.R. Hunt**[3,4] | **Niklas Boers**[5,6,7] | **Bedartha Goswami**[1]

[1]Machine Learning in Climate Science, University of Tübingen, Tübingen, Germany

[2]Machine Learning in Sustainable Energy Systems, University of Tübingen, Tübingen, Germany

[3]Department of Meteorology, University of Reading, Reading, UK

[4]National Center for Atmospheric Science, University of Reading, Reading, UK

[5]Earth System Modelling, School of Engineering & Design, Technical University of Munich, Munich, Germany

[6]Potsdam Institute for Climate Impact Research, Potsdam, Germany

[7]Department of Mathematics and Global Systems Institute, University of Exeter, Exeter, UK

Correspondence
Felix M. Strnad, Machine Learning in Sustainable Energy Systems, University of Tübingen, Germany.
Email: felix.strnad@uni-tuebingen.de

Abstract

The Indian Summer Monsoon (ISM) and the West African Monsoon (WAM) are dominant drivers of boreal summer precipitation variability in tropical and subtropical regions. Although the regional precipitation dynamics in these two regions have been extensively studied, the intraseasonal interactions between the ISM and WAM remain poorly understood. Here, we employ a climate network approach based on extreme rainfall events to uncover synchronously occurring extreme rainfall patterns across the two monsoon systems. We reveal strong synchronization of extreme rainfall events during the peak monsoon period in July and August, linking heavy rainfall over North India to that over the Sahel with a lag of around 12 days. We find that La Niña like conditions in combination with the Boreal Summer Intraseasonal Oscillation (BSISO) and an enhanced Tropical Easterly Jet (TEJ) foster the synchronization between the ISM and the WAM. The northward-propagating BSISO triggers African Easterly Wave activity, bounded between a reduced African Easterly Jet and the TEJ. These induce westward-traveling anomalous deep convection over the Sahel, which causes extreme rainfall events to occur.

KEYWORDS

climate networks, extreme rainfall events, intraseasonal variability, North India, Sahel, synchronization, teleconnections

1 | INTRODUCTION

The Indian Summer Monsoon (ISM) and the West African Monsoon (WAM) are primary drivers of boreal summer precipitation variability in tropical and subtropical regions. The ISM is characterized by a strong meridional overturning circulation, with a low-level monsoon flow from the Indian Ocean to the Indian subcontinent and a return flow at upper levels known as the northward migration of the Intertropical Convergence Zone (ITCZ: (Bordoni & Schneider, 2008)). Similarly, the WAM is characterized by low-level inflow of moist air from the Atlantic Ocean, which converges with the dry, hot air from the Sahara desert. Both the North Indian and Sahel regions exhibit substantial variations in monsoon rainfall known as "active" and "break" phases (Annamalai & Slingo, 2001; Rajeevan et al., 2010; Hall & Peyrillé, 2006). The active phase is often associated with extreme rainfall events (EREs), which can have severe socioeconomic impacts (Kotz et al., 2022).

The intraseasonal variability comes about through a complex interplay of tropical and subtropical large-scale modes of variability (Priya et al., 2015; Sooraj et al., 2020; Nikumbh et al., 2023). For example, the rainfall dynamics in both North India and the Sahel are known to be correlated with the intensity and location of the Tropical Easterly Jet (TEJ: (Huang et al., 2019)). The TEJ is a strong zonal wind maximum in the upper troposphere that is located over the tropical Indian Ocean and is mainly present during boreal summer months (June–September). It is established due to the meridional temperature gradient between the Equatorial Indian Ocean and the Asian landmass and extends from the Pacific Ocean to the west coast of the Sahel (Koteswaram, 1958). Elevated heating over the Tibetan Plateau increases this gradient and leads to an enhancement of the TEJ. Previous studies have found a strong connection between the strength of the TEJ and ISM rainfall (Pattanaik & Satyan, 2000; Madhu, 2014; Huang et al., 2019, 2021). Through latent heat release aloft, which again strengthens the meridional temperature gradient, the TEJ becomes stronger (weaker) during wet (dry) years of the ISM (Sathiyamoorthy et al., 2007; Rao & Srinivasan, 2016). Conversely, a stronger upper-level jet increases the vertical wind shear, which in turn leads to more convective organization and also enhances the northward migration of the ITCZ to the Indian subcontinent (Jiang et al., 2004; Bickle et al., 2021). This consequently increases rainfall in India. The physical mechanism underlying the link between the TEJ and Sahel rainfall is less well understood, even though the strong statistical correlation between the TEJ and Sahel rainfall is well documented and consistent over several decades (Grist & Nicholson, 2001; Sathiyamoorthy, 2005; Nicholson, 2008).

The TEJ often extends over Africa, sitting above the lower-level African Easterly Jet (AEJ). Within the AEJ, African Easterly Waves (AEWs) are embedded, which cause around 90% of the annual rainfall in the Sahel region (Nicholson, 2013). AEWs grow from thermal disturbances, triggered mainly by anomalous convection (Thorncroft et al., 2008). The zonal TEJ and AEJ supply the energy to the AEWs (Skinner & Diffenbaugh, 2013). Mesoscale convective systems are often embedded in the tracks of these waves (Hamilton et al., 2020) and play an important role in the occurrence of EREs in the western Sahel (Nicholson et al., 2008). Several studies have shown that wet years in the Sahel are often characterized by a regionally stronger TEJ, even on interannual time-scales (Nicholson & Klotter, 2021). A strong TEJ is conducive to wet conditions over West Africa and recent work has also shown that there is only a weak relationship between TEJ variability and daily variations in convection over the Sahel (Lemburg et al., 2019; Nicholson & Klotter, 2021). Therefore, Lemburg et al. conclude that the intensity of the TEJ is not influenced by rainfall variations over Northwest and Central Africa. Bickle et al. (2021). show that increased vertical shear in the Sahel region also modulates the occurrence of rainfall. Further, Whittleston et al. (2017). showed that the coupling of the different zonal jets (TEJ, AEJ, and AEW activity) over West Africa and the Sahel together modulate the rainfall, but also the majority of climate models fail to capture the observed relationship between the jets and Sahel rainfall.

While the TEJ is influenced by strong convection over India, the occurrence of EREs in the Indo-Pacific region itself is substantially influenced by a large-scale mode of convective variability, at time-scales between 30 and 60 days: the Boreal Summer Intraseasonal Oscillation (BSISO: (Kikuchi, 2021)), sometimes also referred to as the Monsoon Intraseasonal Oscillation (MISO: (Webster, 2020; Nikumbh et al., 2021)). Wang & Sobel (2022). demonstrated that its propagation characteristics can be derived from the same principles as the better known Madden–Julian Oscillation (MJO: Madden & Julian (1971)), which is the dominant mode of intraseasonal variability on the global scale (Zhang, 2005; Zhang et al., 2020). The BSISO can thus be regarded as the summer counterpart of the MJO and is sometimes also called the summertime MJO (Chang et al., 2021). The BSISO originates in the Indian Ocean and propagates northeastward across India, the Maritime Continent, and the Western Pacific (Kikuchi et al., 2012; Lee et al., 2013; Kiladis et al., 2014). This oscillation plays a crucial role in the generation of deep convection and interacts with the local circulation patterns over the Indian subcontinent, for example, by modulating the frequency and behavior of low-pressure systems (Hunt & Turner, 2022)

and modulating the occurrence of EREs (Nikumbh *et al.*, 2021).

The WAM also shows variability on the same time-scale (Matthews, 2004; Janicot *et al.*, 2009; Schlueter *et al.*, 2019) and this modulates occurrences of precipitation in the Sahel (Sossa *et al.*, 2017; Vizy & Cook, 2022). Some studies suggest that the initiation of the BSISO via anomalous convection over the Indian Ocean results in eastward-propagating Kelvin waves and westward-propagating Rossby waves (Maloney & Shaman, 2008). Currently, most studies agree that both components (Kelvin and Rossby waves) have a significant impact on the WAM (Mohino *et al.*, 2012; Niang *et al.*, 2017). These Rossby waves exert a modulating influence on the mid-tropospheric temperature structure over the Sahel, thereby facilitating deep convection (Mohino *et al.*, 2012), which in turn triggers AEW activity (Alaka & Maloney, 2012; Ventrice *et al.*, 2011).

The ISM rainfall variability is modulated further, on interannual time-scales, by the El Niño–Southern Oscillation (ENSO). Indian rainfall is enhanced (reduced) during La Niña (El Niño) years, typically explained by the modulation of the Walker circulation (Kumar *et al.*, 2006). The BSISO itself is modulated by ENSO, with La Niña like conditions leading to an intensified northward propagation and more EREs in North India (Strnad *et al.*, 2023). Similarly to the Indian rainfall, a teleconnection between ENSO and Sahel rainfall has been noted (Folland *et al.*, 1986), although the mechanism to explain this connection is controversial (Joly *et al.*, 2007). Modulation of the TEJ by ENSO has been suggested to explain the teleconnection (Chen & van Loon, 1987): due to constructive interference of the Walker circulation in La Niña years, the TEJ intensifies and expands both horizontally and vertically (Nithya *et al.*, 2017), inducing more rainfall over the Sahel. In contrast to this, the TEJ weakens and contracts spatially during El Niño years, leading to a decrease in rainfall over the Sahel (Nithya *et al.*, 2017). This mechanism is used, for instance, to explain why El Niño events reduce rainfall and foster the occurrence of droughts in Ethiopia (Gleixner *et al.*, 2017), and is also present in some global circulation models (Bader & Latif, 2003; Vashisht *et al.*, 2021).

Summarized, the two monsoon systems of the ISM and WAM are both influenced by the same global large-scale modes of variability like ENSO (Shaman & Tziperman, 2007) and the MJO (Matthews, 2004). Further, a direct modulation of the ISM by the tropical Atlantic via atmospheric Rossby waves in the Tropics has been reported (Mohino *et al.*, 2012). However, the occurrence of rainfall in the two monsoon systems of the ISM and WAM is commonly still investigated mainly on interannual to decadal time-scales in the framework of the "Global Monsoon" (Wang & Ding, 2008; Geen *et al.*, 2020). Possible interactions between both monsoon systems on intraseasonal time-scales, however, have not been investigated systematically. In their study, Boers *et al.* (2019). reveal a synchronization pattern of EREs between North India and the Sahel on daily time-scales. Some teleconnections of the ISM shown in Boers *et al.* (2019). have been explained in recent years; for example, the dynamical mechanism linking the ISM to the Maritime Continent (Strnad *et al.*, 2023), circumglobal teleconnection (Beverley *et al.*, 2019, 2021), or the Yellow River Basin (Gupta *et al.*, 2022). However, the reasons for the synchronization between the ISM and WAM remain unclear. Our study thus aims to identify the atmospheric processes that drive the synchronization between the ISM and the WAM on a time-scale of multiple days.

Previous studies on rainfall variability during the boreal summer monsoon have traditionally used methods such as linear regression, empirical orthogonal functions (EOFs), and composite analyses (Ding & Wang, 2005, 2007; Wang & Ding, 2008; Vellore *et al.*, 2014; Walker *et al.*, 2015). These are not suitable to capture the spatial characteristics of EREs. Additionally, the identification of specific and possibly varying time lags associated with particular interaction patterns of different atmospheric processes is challenging. Therefore, in this study, we examine the spatial patterns associated with EREs that occur concurrently in the Tropics and subtropics by employing a climate network approach (Tsonis & Swanson, 2008; Malik *et al.*, 2010; Boers *et al.*, 2014, 2019; Strnad *et al.*, 2022, 2023). Climate networks are networks where links reflect a strong statistical correlation between corresponding nodes, typically representing time series from different spatial locations. Here, the correlation is accessed by quantifying the synchronicity of EREs using the event synchronization algorithm (Quian Quiroga *et al.*, 2002). We adopt the methodology introduced in Strnad *et al.* (2023). to identify groups of densely connected nodes in the network, referred to as communities. These can be understood as spatial regions where EREs occur significantly synchronously.

Our method uncovers a community of synchronous EREs comprising North India, China, and the Sahel region. We then investigate the mechanisms responsible for the synchronization by building upon the method from Schlör *et al.* (2024)., clustering the propagation of EREs in a multivariate latent space. Our approach reveals a robust time-lagged connection between the ISM and WAM monsoon regions, prompting a subsequent exploration using traditional meteorological analysis tools. We show in the following that the aforementioned large-scale modes of variability, namely the BSISO, TEJ, and ENSO, interact to foster the synchronization between the ISM and the WAM.

2 | DATA AND METHODS

2.1 | Data

This study focuses on the analysis of EREs occurring within the monsoon season, set as June–September (JJAS). Consequently, the analysis is limited to this specific time frame.

2.1.1 | Precipitation data

We use the 0.25° daily resolved precipitation data from the Multi-Source Weighted-Ensemble Precipitation (MSWEP) dataset (Beck *et al.*, 2019b) for the period 1980–2022. The MSWEP dataset is chosen for its longer time range compared with other available multi-satellite precipitation products, improving statistical robustness. It has been shown to represent high rainfall quantiles well on global scales (Beck *et al.*, 2019a). We restrict our analysis in the meridional direction to the latitudinal range from the Southern subtropics to the Northern midlatitudes (180°W–180°E, 30°S–70°N, see Figure 1a).

2.1.2 | Extreme rainfall events

We generate binary event series from the precipitation dataset. We only consider "wet days", defined as days with a rainfall sum of at least 1 mm. Events are pointwise-defined: we determine one ERE day as a day on which the daily precipitation sum exceeds the 90th percentile ($Q_{0.9}(\cdot)$) of all wet days at that specific location (Figure 1b). This results in one binary time series
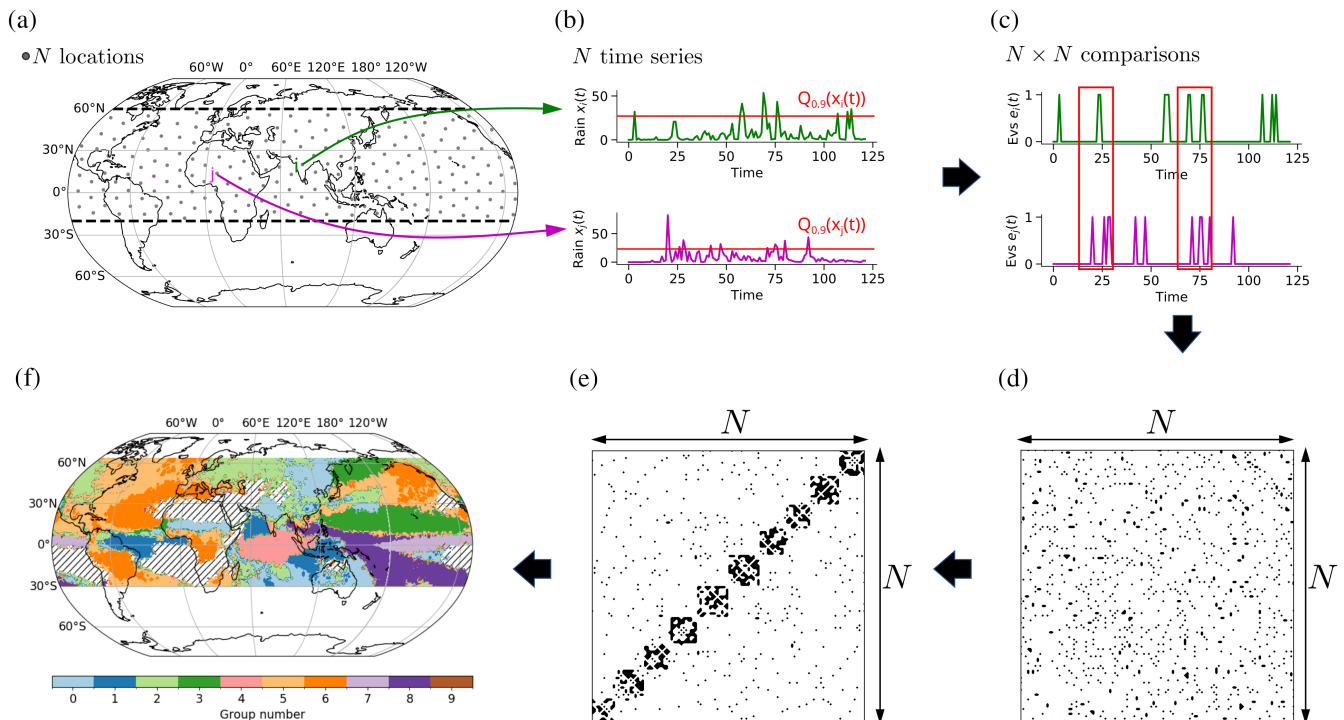

FIGURE 1 Schematic of the community detection approach. (a) The climate network is constructed by mapping the data to a spatial grid of N approximately uniformly distributed points using the Fekete algorithm (Bendito *et al.*, 2007). For visualization purposes, only every 10th grid point is plotted. Dashed lines indicate the latitudinal range of the analysis [20°S, 60°N]. (b) Every grid point is associated with a precipitation time series. By thresholding locally at the 90th percentile ($Q_{0.9}$), we obtain a binary event series (*Evs*). (c) The event synchronization algorithm (Quian Quiroga *et al.*, 2002) is employed to evaluate the statistical dependences between all pairs of time series (i.e., a total of $N \times N$ comparisons). The time series and event series in (b) and (c) are just for illustrative purposes. (d) The adjacency matrix **A** of the network characterizes the linkages between nodes, delineating the network's underlying topology. Each black dot represents a statistically significant synchronization between two nodes. Again, this matrix is for illustrative purposes. (e) Communities are detected by identifying blocks in the adjacency matrix **A** via reordering of rows and columns using a probabilistic community detection algorithm. Communities within the climate network represent groups of nodes characterized by stronger internal connectivity compared with their connections with nodes outside the community. (f) The block structure is projected back to the spatial map. Nodes that are assigned to the same community are colored in the same color. The hatched areas indicate regions with only a few wet days, which are excluded from the analysis. [Colour figure can be viewed at wileyonlinelibrary.com]

per grid point, where 1 indicates an event and 0 indicates no event.

2.1.3 | Reanalysis data

To analyze large-scale patterns associated with the synchronization, we use the following variables from the ERA5 Global Reanalysis dataset (Hersbach *et al.*, 2020): daily outgoing longwave radiation (OLR), sea-surface temperature (SST), and horizontal (U, V) wind fields, and vertical velocity ω, specific humidity q, and temperature T on pressure levels from 50 to 1000 hPa in steps of 50 Pa. The datasets used for the multivariate principal component analysis (PCA) are interpolated onto a $1° \times 1°$ grid, and all remaining datasets are interpolated onto a $2.5° \times 2.5°$ grid. To ensure the robustness of our analysis and to avoid confounding effects from long-term climate change, we apply a linear detrending to all reanalysis datasets.

2.1.4 | ENSO index

The ENSO state is obtained using the multivariate ENSO index version 2 (MEIv2: (Wolter & Timlin, 2011)). The MEIv2 is a multivariate index that combines six observed variables over the tropical Pacific Ocean to provide a comprehensive measure of the ENSO state, obtained from the National Oceanic and Atmospheric Administration (NOAA) Physical Sciences Laboratory (PSL).[1]

2.1.5 | BSISO index

The daily resolved BSISO index by Kikuchi *et al.* (2012). is taken from https://iprc.soest.hawaii.edu/users/kazuyosh /Bimodal_ISO.html (last accessed: May 10, 2023). The index consists of two time series BSISO1 and BSISO2. The amplitude, given by $A = \sqrt{\text{BSISO1}^2 + \text{BSISO2}^2}$, defines an active (inactive) BSISO by $A \geq 1$ ($A < 1$) (Wheeler & Hendon, 2004). The two-dimensional phase space spanned by BSISO1 and BSISO2 is subdivided into eight equally sized sections that denote the phase of the BSISO.

2.1.6 | Tropical Easterly Jet index

We employ the index definition of Huang *et al.* (2019). to describe the characteristics in terms of amplitude and variability of the TEJ for the period from June–September. The metric of this index, denoted as the Tropical Easterly Jet Index (TEJI), is mathematically formalized by spatially averaging the U-wind anomalies at the 200-hPa pressure level enclosed in the box within the interval [0°E, 70°E], [0°N, 15°N] (magenta box in Figure S9 in the Supporting Information (SI)). We define enhanced (reduced) phases of the TEJI as events exceeding one standard deviation below (above) the mean (as the jet flows westward, the zonal wind values are negative: see Supporting Information Figure S9).

2.1.7 | All India rainfall index

The All India rainfall index (AIRI) by Parthasarathy *et al.* (1994)., available from the India Meteorological Department (IMD),[2] is used to represent the ISM rainfall variability in JJAS. We consider days above (below) one standard deviation from the mean as active (break) ISM days.

2.2 | Communities of synchronous extreme rainfall events

We use climate networks to determine regions of significantly synchronously occurring EREs. This involves multiple analysis steps, visualized schematically in Figure 1.

2.2.1 | Mapping to a grid of spatially uniformly distributed points

On a regular (rectangular) grid on a sphere, the distance between grid points decreases the closer they are to the poles, and they are therefore also more likely to be correlated. This could cause biases in the community detection algorithm later (see Section 2.2). To avoid these confounding correlation effects, we first map the data to a grid of spatially approximately uniformly distributed points using nearest-neighbor interpolation (Figure 1a) by employing the Fekete algorithm (Bendito *et al.*, 2007). For computational reasons, the distance between two points of the new grid is set to around 111 km, which corresponds to the spatial distance between two points at the equator of a regular Gaussian 1° grid, resulting in a total of approximately 9600 grid points.

2.2.2 | Climate network definition

A spatiotemporal dataset of rainfall time series is denoted as $\mathbf{X} \in \mathbb{R}^{N \times T}$, where N represents the spatial locations and T is the number of time points (i.e., all days in JJAS for the period 1980–2022, that is, in total $T = 5002$). The climate network is then defined as $\mathcal{G} = (V, E)$, where

each geographical location $i \in 1, \ldots, N$ corresponds to a node $n_i \in V$, and is associated with the rainfall time series $\vec{x}_i = (x_{i,0}, \ldots, x_{i,T}) \in \mathbf{X}$. E represents the set of edges within the network. An edge between two nodes n_i and n_j encodes a robust statistical dependence between the time series $\vec{x}_i(t)$ and $\vec{x}_j(t)$ labeled as edge $e_{ij} \in E$.

2.2.3 | Event synchronization

First, all rainfall time series $\vec{x}_i(t)$ are transformed into binary event series $\vec{e}_i(t)$ by thresholding at the 90th percentile of all wet days (Figure 1b; see above). The event synchronization algorithm (Quian Quiroga *et al.*, 2002) is employed to evaluate the statistical dependences between pairs of event series, serving as a metric for quantifying the synchronization between all pairs of time series within the network (Figures 1c, S1). This method involves counting concurrently occurring events within event sequences from different locations, allowing a temporal gap—the so-called dynamical delay τ—between events in these sequences to account for time deviations of at most 10 days (see Supporting Information Section S1). The strength of the synchronization between locations is assessed by summing up synchronous time points across all event pairs. The statistical significance of synchronization between a pair of event series is estimated using a null-model test with 2000 random surrogates for each pair of event series separately (see Supporting Information Section S1, statistical significance). For details, we refer the reader to Supporting Information Section S1 or to the detailed descriptions in Boers *et al.* (2014, 2019); Strnad *et al.* (2023). The adjacency matrix $\mathbf{A}$ of a network characterizes the linkages between nodes, delineating the underlying topology of the network, which can be visualized in the form of a graph. The adjacency matrix is a mathematical representation of these connections and captures the presence or absence of links between nodes expressed as a $N \times N$ matrix, where $A_{i,j} = 1$ indicates that events at location i are statistically significantly co-occurring synchronously with events at location j, and is set to 0 otherwise (Figure 1d).

2.2.4 | Communities of synchronous extreme rainfall events

Communities within the climate network represent groups of nodes characterized by a higher internal density of links compared with their link density with groups of nodes outside the community. Keeping in mind that the network is constructed based on pairs of event series exhibiting statistically significant synchronicity in the occurrence of EREs, these communities correspond to spatial regions where EREs are more likely to occur synchronously. These communities often correspond to spatially connected regions, possibly over large spatial distances (Figure 1f). The assumption is that points within the same community are attributable to one (or even multiple) shared underlying physical mechanism(s) (Strnad *et al.*, 2023). In practice, communities are determined by reordering rows and columns of the adjacency matrix $\mathbf{A}$ to obtain a block structure (Figure 1e). An approach that uses a stochastic block model (SBM) is very common. The SBM serves as a generative model for random graphs, generating community structures—specifically, subsets of nodes referred to as "blocks". These exhibit distinct connectivity patterns, being connected with one another at particular densities of connected nodes. The model implementation used in this work is the network analysis package *graph_tool* (Peixoto, 2014a), favored for its computational efficiency and its probabilistic output. This implementation can infer the optimal number of communities in the data based on the principle of parsimony, that is, simple structures with a low number of communities are preferred to more complex ones with a higher number of communities. In our case, the optimal number of communities for the whole network was determined to be 10. Further, the Bayesian approach of the algorithm makes it possible to quantify the posterior probability of each node belonging to a specific community by sampling different network structures from the posterior distribution. We average over all samples drawn from the posterior distribution and divide it by the total number of samples to obtain a probability between 0 and 1. We call this the membership likelihood of a node to a community. It quantifies the probability of a node belonging to a specific community based on the community structure. For more in-depth details, we refer the reader to Peixoto (2014b, 2019).

2.3 | Lagged synchronous rainfall index

We introduce a synchronization index, denoted as $SRI(t)$, to quantify for two (potentially distinct) sets of nodes A and B of the network their time-dependent level of (lagged) synchronicity in the occurrence of EREs. For each time point t, we count for each node in set A the number of EREs that are followed at a lag τ_{lag} by events in set B. The event series associated with the set A (B) are denoted as $e_n^A(t)$ ($e_m^B(t)$), where n (m) describes the nth (mth) node in A (B) with total number of points N (M). We define the lagged synchronization index $SRI_{\tau_{\text{lag}}}(t)$ for a specific lag τ_{lag} as

$$SRI_{\tau_{\text{lag}}}(t) = \sum_{n=1}^{N} \sum_{m=1}^{M} e_n^A(t) \cdot e_m^B(t - \tau_{\text{lag}}). \quad (1)$$

As we observe further that the lag with the highest synchronization between synchronous events in A and B can vary (e.g., Figure S8a), we thus count all synchronizations between A and B within a certain range of lags $[\tau_{\min}, \tau_{\max}]$. Summing over all possible lags and using Equation (1), we define the synchronous rainfall index SRI as

$$SRI(t) = \sum_{\tau=\tau_{\min}}^{\tau_{\max}} SRI_\tau(t). \quad (2)$$

Counting the number of (lagged) synchronous events per time step enables us to quantify the number of EREs within a set of locations A that are followed by events in a set of locations B within a range of possible lags. To pinpoint further the points in time of exceptionally strong (lagged) synchronization, we compute the 90th percentile of all values of the time series $SRI(t)$ and define these points in time as the *most synchronous days* (MSDs) that are above this threshold.

2.4 | Latent space clustering of propagation pathways

To obtain meaningful clusters of the synchronization pattern, we propose a variation of latent space clustering,

visualized schematically in Figure 2, as has been used in, for example, (Schlör *et al.*, 2024). The latent space is a lower-dimensional representation of the original high-dimensional data space, where the data are projected to capture the most important features (Bishop & Nasrabadi, 2006). The latent model used here is EOF analysis, also known as PCA, which reduces the dimensionality of the data while retaining the largest possible fraction of its original variance. The input data, provided as a spatiotemporal field $x \in \mathbf{X}$, are selected and pre-processed as follows. We assume that the mechanism that drives the synchronization over the Sahel is related to AEW activity, which is known to be responsible for about 90% of precipitation over the Sahel and is strongly influenced by the AEJ (at around 600 hPa), between the TEJ at around 200 hPa and the AEJ at around 600 hPa (Nicholson, 2013). Therefore, the physical mechanism should be reflected in the zonal wind fields over pressure levels from the near-surface towards the upper troposphere. To avoid the curse of dimensionality, we adopt the approach presented by Whittleston *et al.* (2017). The three-dimensional fields of the zonal winds (longitude, latitude, pressure level) are reduced to a two-dimensional (latitude, pressure level) field by averaging over 15°W–15°E (red rectangle in Figure 2). The resulting time series are z-score normalized. The resulting field is then used as input for the PCA.
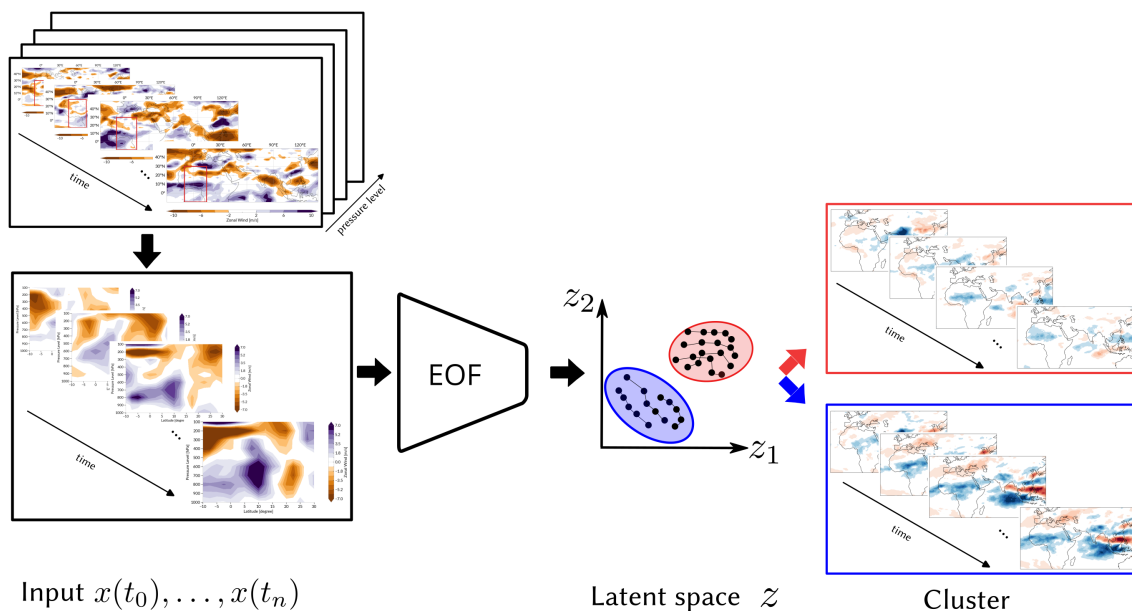

FIGURE 2 Sketch of the latent space clustering. The propagation pathways are clustered via traces in the latent space z. The three-dimensional input field is first reduced to a two-dimensional field by averaging over the zonal range marked by the red rectangle and then transformed to a low-dimensional latent space, which is denoted by the encoder. In our case, the encoder function is a Principal Component Analysis. Input fields, $x(t_1), \ldots, x(t_n)$, for a propagation sample of n consecutive time steps are encoded in the latent space z (displayed as black dots). These build a trace in the latent space (visualized by connected lines). These traces are clustered by a clustering algorithm; the clusters are visualized as red and blue regions in the latent space. The clustered time points can be used to create corresponding composite anomaly maps of any variable in the original (real) space. [Colour figure can be viewed at wileyonlinelibrary.com]

At time t a transformation, $z_t = e(x_t)$, is applied to map the high-dimensional space, $\mathbb{R}^N$, where $N = N_{\text{lat}} \times N_{\text{plevel}}$, to a lower-dimensional space, $\mathbb{R}^M$, with $M \ll N$. To cluster the dynamics up to a lead of +15 days, we compute the traces in the latent space z, where each sample s concatenates the steps in the latent space z from day 0 to day +15: $s = \{z_0, z_1, \ldots, z_{15}\}$. Therefore, each sample t is a vector of length $15 \times n_{\text{EOFs}}$, where n_{EOFs} is the number of EOFs used for the clustering (see SI Section 3). To select the EOFs that represent the propagation pathways best, we consider the EOFs of which the corresponding principal components (PCs) have the highest correlation coefficient with the lagged synchronous index $SRI(t)$ (Equation 2).

We employ the standard k-means clustering algorithm to cluster traces in the latent space z. To determine the optimal number of clusters, we use the silhouette score (Rousseeuw, 1987). We remove consecutive days of the MSDs to obtain meaningful traces. The silhouette score measures the similarity of an object to its own cluster compared with other clusters, ranging from -1 to 1. A high value indicates a strong match to its cluster and a poor match to neighboring clusters. A high average silhouette score across all samples indicates an appropriate clustering configuration. We performed a grid search over the number of clusters and EOFs, ranging from 2 to 10 clusters and 1–10 EOFs, in order to identify the optimal clustering configuration. Here, the best clustering is obtained for two clusters and a single EOF with an overall silhouette score of 0.4. Single samples with a silhouette score below 0.1 are excluded from the analysis.

2.5 | Estimation of conditional probabilities

The probability that a day is a day belonging to the MSDs (i.e., days for which we observe a high number of synchronizations between North India and the Sahel, see Section 2.3) under a condition, a (e.g., the condition that the SST state in the tropical Pacific fulfills a La Niña condition), is calculated as follows. Let s be the condition that a day belongs to the set of MSDs S and a be a particular condition, where the set of days fulfilling the condition a is denoted as A. Then

$$P(s|a) = \frac{P(s,a)}{P(a)} = \frac{||S \cap A||}{||A||}$$

describes the conditional probability for synchronous events under condition a, where $P(s,a)$ is the joint probability of s and a and $P(a)$ the probability of a. Here, $|| \cdot ||$ denotes the set cardinality and $S \cap A$ the intersection of days in S and A, that is, all days that are MSDs and fulfill condition a. Accordingly, the conditional probability for a

further, second condition b that fulfills all days in the set of days B is computed as

$$P(s|a,b) = \frac{P(s,a,b)}{P(a,b)} = \frac{||S \cap A \cap B||}{||A \cap B||}. \tag{3}$$

This procedure is analogous for further conditions c, d, etc. In our case, the conditional probabilities are estimated for MSDs conditioned on the ENSO state, the BSISO phase and activity, and the TEJ state. A corresponding null model is estimated by assuming that the MSDs are randomly distributed over time. The null model probability of a day being an MSD is then calculated by dividing $||S||$ by the total number of days, weighted by the relative occurrence of a condition a over time.

3 | RESULTS

3.1 | Lagged extreme rainfall synchronization between North India and the Sahel

3.1.1 | Pattern of the synchronization

The application of the community detection algorithm (see Section 2.2) to the global climate network reveals 10 regions of synchronous EREs (Figure 1e). The objective of the network analysis is to identify the regions that are connected by the synchronization of EREs. These regions constitute a "community" within the climate network, constructed by estimating patterns of simultaneously occurring EREs in a domain restricted to the Tropics and boreal subtropics (see Figure 1 and Supporting Information Section S1 for details). Each of these communities could be investigated on its own, given that they extend over extensive spatial scales and are characterized by a high membership likelihood of the nodes in the respective regions belonging to the community (Figure S2). This study focuses on the community that encompasses North India, including the Indo-Gangetic Plain, the Himalayan foothills (NI, red contour in Figure 3a), East Asia (EA, pink contour in Figure 3a) delineated by the Himalayan mountain chain, and the Sahel Zone (SZ, green contour in Figure 3a) bounded between the tropical rainforest and the Sahara desert. This community is characterized by a high membership likelihood of the nodes in the respective regions belonging to the community. The high spatial coherence indicates that the community is a stable manifestation of the synchronization pattern associated with synchronous EREs (Figure S2). The synchronization between NI and EA has been analyzed in previous studies and can be attributed to the Eurasian Wave Train associated with the Silk Road pattern (Gupta *et al.*, 2022).
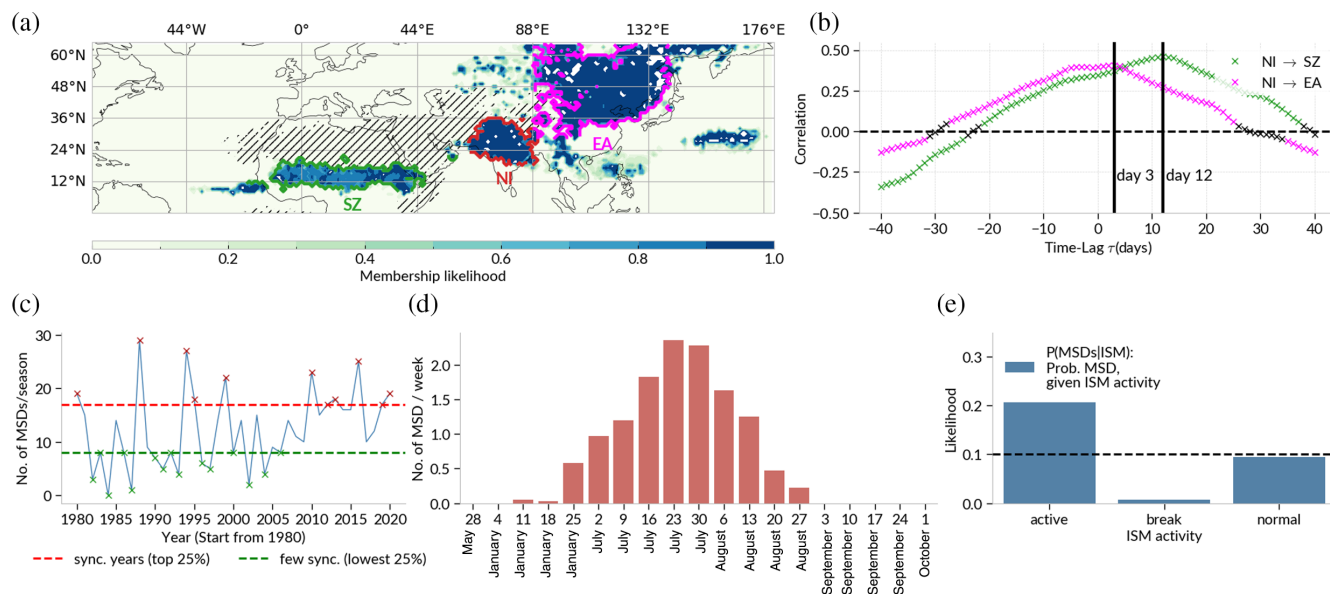
FIGURE 3 Synchronization pattern of extreme rainfall between North India and the Sahel. (a) Regions of statistically significant synchronization between spatial locations are plotted according to their membership likelihood of being in the community comprising North India (NI, red contour) and the Sahel Zone (SZ, green contour). The communities are determined using a probabilistic hierarchical community detection algorithm based on the stochastic block model and overlaps of 100 independent runs (see Section 2.2). Hatched areas indicate regions with few wet days (i.e., locations with less than 10 rainy days in 40 years), which are excluded from the analysis. We find a community that comprises the regions of North India (NI), East Asia (EA), and the Sahel Zone (SZ). The connection between NI (red contours), SZ (green contours), and EA (magenta contours) is investigated. (b) Lead–lag correlations in steps of days between time series obtained from counting the number of extreme events of locations in the NI and the SZ (green line) and NI and EA (magenta line). Only correlations with $p < 0.001$ are considered significant and are shown by colors, while black crosses denote non-significant correlation. The maximum correlation is marked by a vertical solid line. (c) Interannual variability of the synchronization between NI and SZ is displayed by counting the number of MSDs per JJAS season. (d) For the MSDs, we estimate the distribution over the week of the year in the JJAS observation period. (e) The occurrence of MSDs is conditioned on the ISM activity. The dashed line indicates the null model of randomly distributed MSDs per season. [Colour figure can be viewed at wileyonlinelibrary.com]

The time lag between NI and EA of three days (Figure 3b, pink line) is consistent with the propagation speed of the Eurasian Wave Train and the results in (Gupta *et al.*, 2022). In the following, we focus on exploring why the EREs manifest synchronously (within a certain time range) over the large continental-scale distance between North India (red contour in Figure 3a) and the Sahel Zone (green contour in Figure 3a).

3.1.2 | Time lags of the synchronization

Synchronizations were observed to peak in strength at a time lag of around 12 days, on average, throughout boreal summer (June, July, August, September: Figure 3b). This characteristic time delay between EREs within the NI region and the SZ locations is estimated by lead–lag correlation analysis. The number of occurrences of synchronization patterns between NI and SZ is not constant but varies substantially between different years (Figure 3c). We obtain this yearly fluctuation by counting the number of MSDs per year. For later reference, we mark the

lowest 25% as the least synchronous years (red markers in Figure 3c). We also observe that synchronization occurs mainly during the core monsoon season from July–mid-August (Figure 3d). The distribution over the JJAS period is estimated by the week of the year for all MSDs identified. Therefore, hereafter we focus on synchronization events in July and August (JA), which we consider to be the background state under which most synchronization happens. While the occurrence of synchronous events is high mainly during July and August, coinciding with the period of highest daily rainfall sums in India, there is still strong day-to-day variability within these months.

3.2 | Distinct synchronization patterns with varying strength

The synchronization between North India and the Sahel is not instantaneous but lags by almost two weeks (Figure 3b) and varies across years (Supporting Information Figure S8a) with varying SST background state in the

tropical Pacific (Supporting Information Figure S8b–d). We thus investigate potential reasons for the variations of the synchronization patterns.

To obtain a meaningful classification of the MSDs, we apply a clustering approach. We expect that the synchronized events in SZ are somehow driven by the convective activity induced through AEWs. This motivates the choice of the following input variables for a PCA-based clustering (see Section 2.4). We use zonal U-wind fields over all pressure levels from the surface up to 100 hPa to capture changes in the structures of the associated AEJ and TEJ that act as boundaries for the occurring AEWs. Where clusters of consecutive days occur in the set of MSDs, we remove all but the first day to avoid including the same event more than once in our composite. The PCA helps to reduce the dimensionality of the fields substantially and to identify the PCs of the vertical wind structure that are associated with the synchronization (see Section 2.4 for details). We create a trace in the latent space of 12 consecutive days (in steps of 2 days) for each time point that is identified as a MSD. These traces are used as input features for a k-means clustering algorithm. The clustering with the highest silhouette score (≈ 0.4) is obtained for $k = 2$ clusters and one EOF (Figure 4). For reference, the resulting clusters can be found in the supplementary material (S3). The clustering approach is robust. An alternative approach using a multivariate PCA (MV-PCA) yields similar results (Supporting Information Figure S7). We thus find two distinct clusters of MSDs. The years in which these clusters occur are largely distinct from each other in terms of timing (Figure S12).

We can use these clustered time points to create composite anomaly maps of any variable in the original (geographical) space. We create composite anomaly maps for the OLR and the vertical velocity at 500 hPa to uncover the time development of the synchronization pattern (Figure 4). We observe that the propagation of negative OLR anomalies is accompanied by a strong rising motion of the air in the mid-troposphere (Figure 4a–h). Composite anomaly maps are computed for each cluster individually in steps of +4 days (Figure 4), revealing two different synchronization patterns:

- **Strong synchronization.** The first column in Figure 4 demonstrates the propagation of anomalous OLR in steps of 4 days, from day 0 to day 12. Note that negative OLR anomalies often coincide with intense rainfall. For day 0, we see a region of negative OLR anomalies peaking over North India and ranging towards East Africa around the Ethiopian Highlands (Figure 4a). For day +4, these are largely confined to North India and re-emerge later in the Sahel (Figure 4c). Strongly anomalous OLR values over the full range of the Sahel

are observed from around day +8 onwards (Figure 4e). The associated rainfall in the Sahel lags the rainfall in North India by around 10–12 days when the convective anomalies reach the Western African coast (Figure 4g).

- **Weak synchronization.** The second column of Figure 4 does not show a clear propagation pattern over the Sahel and the anomalies are of reduced intensity. Not only the intensity but also the speed of the westward propagation over the Sahel are substantially different from those of the first cluster. We find some anomalously enhanced OLR values around day +12 over the center of the Sahel (Figure 4h). The rainfall over the Sahel lags the rainfall in North India by around +12–15 days.

As the first cluster shows a more intense synchronization pattern and the number of samples in the first cluster is roughly twice the number of samples in the second cluster, we suggest that the first cluster is the main manifestation of the mechanism resulting in the synchronization between NI and SZ, while the second cluster is a weaker variation of the main mechanism. Further, given the smaller cluster size, we cannot rule out that some reasonable fraction of events are not causally connected but arise by chance. Therefore, in the following, we will focus on the first cluster, called the "strong synchronization" cluster.

3.3 | Background conditions favoring ISM–WAM synchronization

The question arises as to why there is such pronounced interannual variability in the synchronization between North India and the Sahel (Figure 3c). We first note that the synchronization is linked to the ISM variability, as the likelihood of occurrence of the MSD is greater in active ISM years, while there are hardly any synchronizations during break ISM events and normal years correspond more or less to the null mode (Figure 3e). To get a clearer understanding of the initiation mechanism, we thus investigate different conditions influencing the variability of ISM activity.

3.3.1 | Anomalous convection in the northwest of India

The synchronization is initiated by anomalously strong convection in northwest India (Figures 4a, 5a). We observe two characteristics. Firstly, the anomalously strong convection in the northwest also coincides with the locations where the strongest rainfall occurs (Figure 5b,d), as
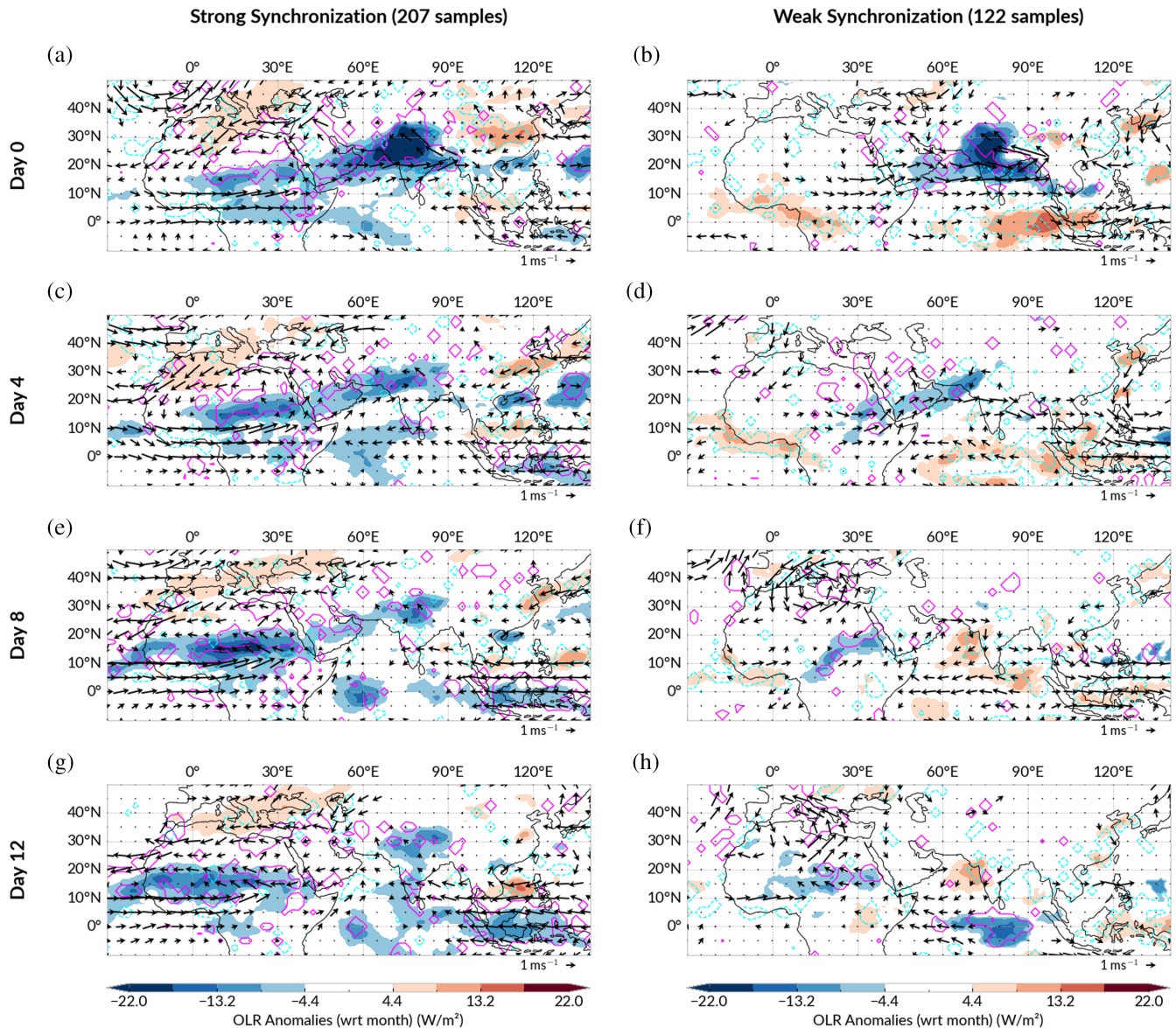
Strong Synchronization (207 samples)   **Weak Synchronization (122 samples)**

FIGURE 4   Propagation for OLR and vertical velocity. We cluster the synchronization patterns based on the most synchronous days using the lagged synchronous index (see Section 2.3). The first column (a,c,e,f) shows the first cluster of the synchronization pattern using OLR. The second column (b,d,f,h) shows the second cluster. We create composite anomaly maps (estimated with respect to the month of the year) for days −4 to +12 OLR in shading, overlapped by anomalous vertical velocity ω at 600 hPa (measured in Pa·s⁻¹) in magenta line contours denoting anomalously rising (sinking) air with ω anomalies larger (smaller) than 1 Pa·s⁻¹. Arrows denote the near-surface horizontal anomaly wind field at 800 hPa. Colored areas, contours, and wind vectors imply statistical significance at 95% confidence level. [Colour figure can be viewed at wileyonlinelibrary.com]

is usually expected in the Tropics. Secondly, we also note a deepening of the monsoon trough for the band of enhanced negative OLR anomalies at around 15°N (Figure 5a). We further observe a strong anomalous moistening of the upper atmosphere in Figure 5b,d, as well as anomalous easterly zonal winds in the upper atmosphere around 200 hPa.

At the same time, the anomalously strong convection in northwest India already shows a typical BSISO (the "summertime MJO") type signal, characterized by

a meridional dipole pattern of OLR anomalies that moves northward (Figures 4a,c, 5a). An analysis based on conditional probabilities (see Section 2.5) supports this impression and shows a substantially increased likelihood for MSDs when the BSISO is in phases 6 and 7 (Figure 5c, Supporting Information S15e). The convective band is thus likely to be associated with the active phase of the BSISO, which is characterized by heavy rainfall (see e.g., Kikuchi (2021); Strnad et al. (2023)).
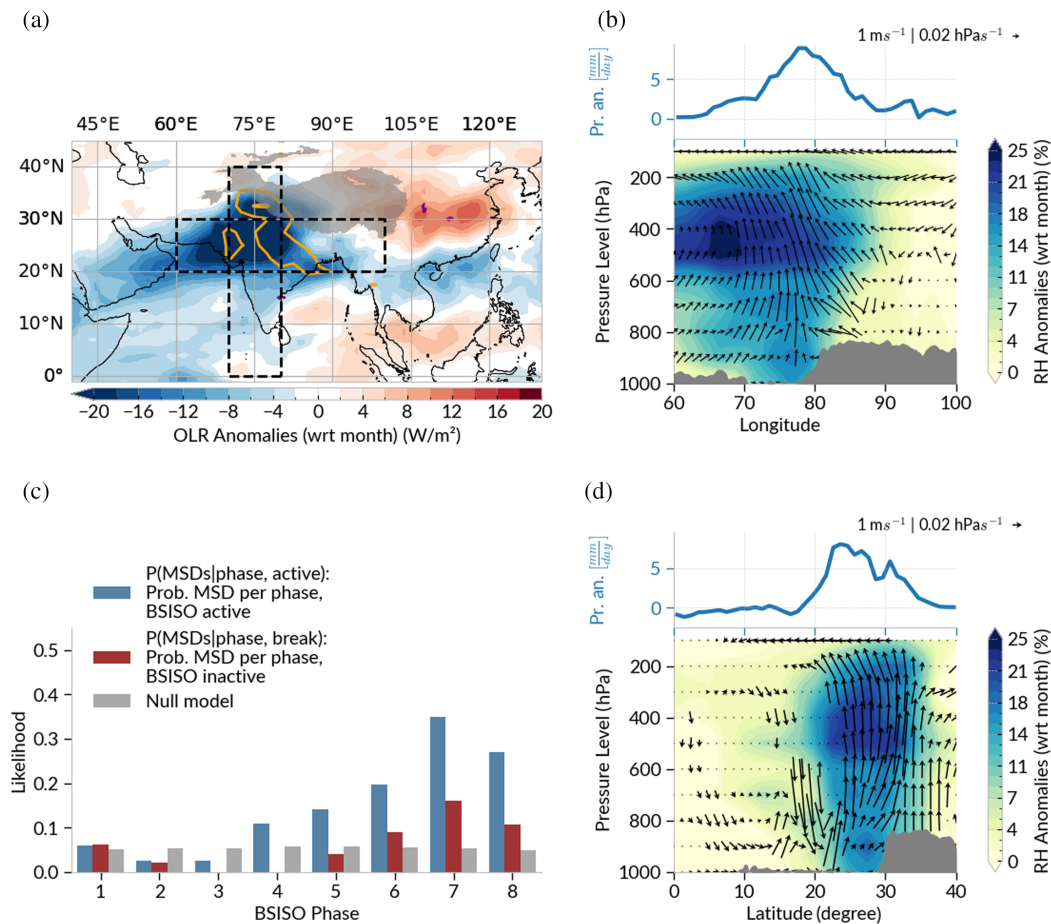
FIGURE 5 Convective anomalies in North India. (a) Composites of the strong synchronization cluster for the OLR superimposed with the vertical velocities ω at 400 hPa (measured in Pa·s^{-1}) in colored contours. Orange solid (purple dashed) contours denote anomalously rising conditions for regions with anomalies larger (smaller) than 3 Pa·s^{-1}. Gray shading represents the Himalayan mountains. We visualize the (b) zonal and (d) meridional circulation averaged over 20°N–30°N (70°E–80°E), shown by dashed rectangles in (a). All composites are computed for the conditions on day 0. Panels (b) and (d) are split into two parts: on top the meridionally (zonally) averaged precipitation anomalies (with respect to the month) are displayed; on the bottom, the vertical circulation is shown by composites of relative humidity anomalies, computed with respect to the month (shading) and wind field anomalies (arrows). The black rectangles in (a) denote the regions for which the vertical circulation plots are calculated. In (a), (b), and (d), colored areas imply statistical significance at a 95% confidence level (otherwise white) using a two-sided t-test. Gray filled contours show the highest 10% of the orography, visualizing the Himalayan mountain chain. The wind fields in the zonal (meridional) circulation plots are estimated using the meridionally (zonally) averaged U (V) anomalies, measured in m·s^{-1}, and the vertical velocity ω in the horizontal direction, measured in hPa·s^{-1}. Only statistically significant arrows at a 95% confidence level using a two-sided t-test are shown. (c) The condition probabilities (Section 2.5) of the selected days conditioned on active (inactive) BSISO phases marked by blue (red) bars. The gray bars denote the likelihood of a respective null model that distributes the MSDs randomly over the BSISO phases with respect to the relative occurrence of each phase. [Colour figure can be viewed at wileyonlinelibrary.com]

3.3.2 | SST background state enhancing synchronization likelihood

We find that the background SST state shows distinct patterns for the two clusters. The strong synchronization cluster shows an anomalous cooling in the central Pacific (Figure 6a)—a La Niña like pattern—and a band of anomalously warm SSTs in the northwest Pacific at around 40°N, which is known as the Kuroshio–Oyashio extension (Di Lorenzo et al., 2023; Joh et al., 2023). Together, these patterns in the Pacific Ocean resemble the patterns

of a negative phase of the Pacific Decadal Oscillation (PDO) in JJAS (see Figure S11). We find that, starting from around 1986, occurrences of samples that are clustered as strong synchronization (weak synchronization) are aligned well with the negative (positive) phase of the PDO (Figure S12). The negative phase of the PDO favors the occurrence of La Niña events (Di Lorenzo et al., 2023). La Niña like conditions lead to an anomalously wet monsoon season in North India, by modulating the Walker circulation (Xavier et al., 2007) and assisting the northward propagation of the BSISO towards the north of India
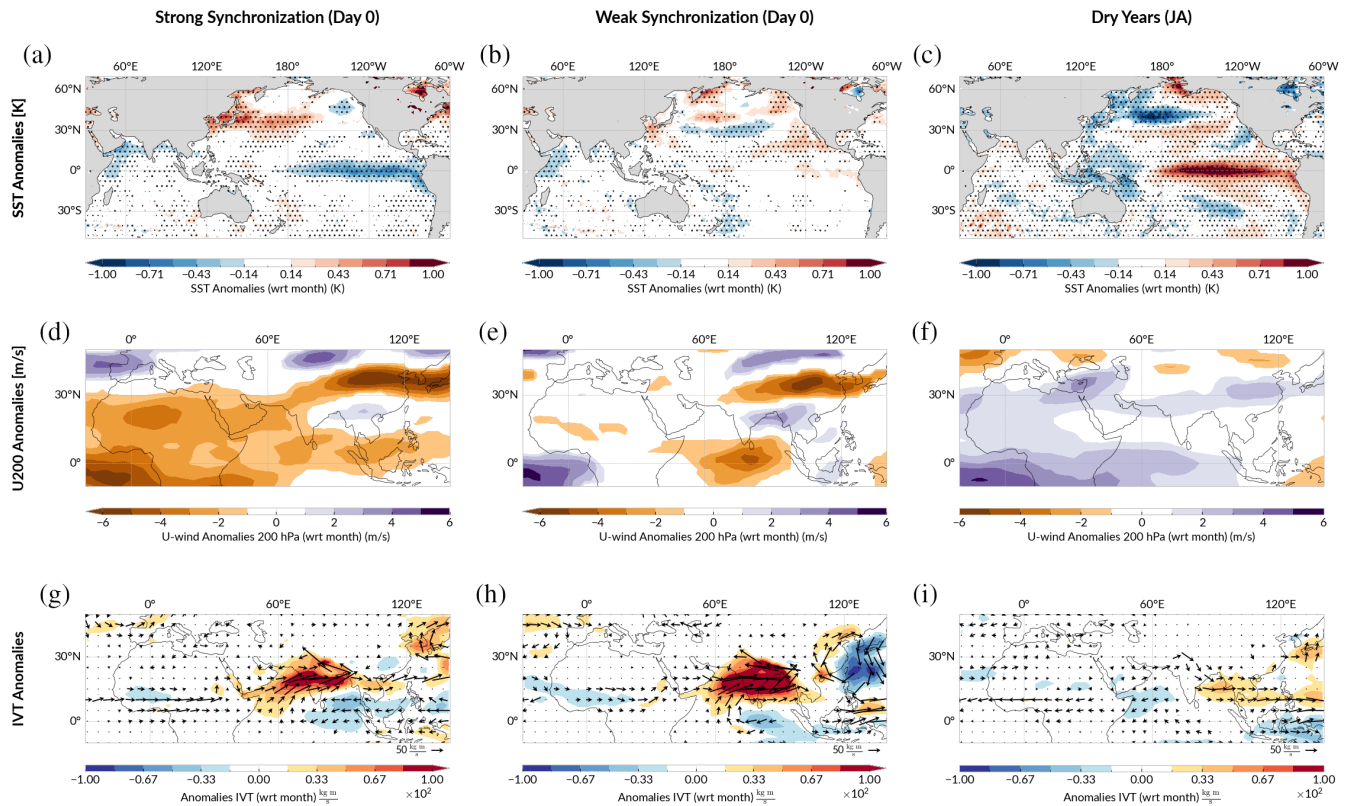
FIGURE 6 Background states for propagation clusters. We visualize different conditions for the samples of days classified as most synchronous days that were clustered (Figure 4) into strong synchronization (first column) and weak synchronization (second column). For comparison, conditions in July–August (JA) for years with few/no synchronizations (see Figure 3c) are also shown (third column). The first row (a–c) shows SST anomalies. The second row (d–f) shows the composited zonal *U*-wind anomalies at 200 hPa. The third row (g–i) shows the integrated vapor transport (IVT) anomalies; arrows denote the corresponding east- and northward components. All composited anomalies are computed with respect to the month of the year. In all panels, colored areas imply statistical significance at 95% confidence level using the Student's *t*-test. The significance for the wind arrows is computed separately for the *U* and *V* components and a wind arrow is shown only if both components are statistically significant. [Colour figure can be viewed at wileyonlinelibrary.com]

(Strnad *et al.*, 2023). We additionally observe associated cool SSTs over the Arabian Sea and the Bay of Bengal, which are probably due to the enhanced convection over the region, that is, cooling the surface through increased insolation and precipitation. This pattern might also be associated with a negative Indian Ocean Dipole, which is often dynamically linked to La Niña events (Meyers *et al.*, 2007; Cherchi & Navarra, 2013). The second cluster does not show a strong SST pattern in the tropical Pacific Ocean (Figure 6b). We identify a weak warming pattern in the Eastern Pacific represented by anomalously warm SSTs in the Pacific Ocean (Figure 6b). However, this pattern is less pronounced than the La Niña like one, suggesting that the La Niña background state provides an important intensification of the synchronization, even if the synchronization can also occur without a La Niña event. For years with only a few synchronizations, which we call dry years, we identify a more pronounced El Niño like pattern represented by anomalously warm SSTs in the central equatorial Pacific Ocean (Figure 6c). This is consistent with the

observation that central Pacific El Niño events are more often associated with a weakening of the Indian monsoon (Kumar *et al.*, 2006; Fan *et al.*, 2017) and thus, in turn, also weaken the synchronization between North India and the Sahel.

3.3.3 | Anomalously strong tropical easterly jet enhances the synchronization

The composite wind field at 200 hPa for the strong synchronization cluster shows an established anomalous corridor that connects the area around the Yellow River Basin zonally with North India and SZ (Figure 6d). The flow is guided by the orography of the Tibetan Plateau and the pattern is especially prominent to the south of the Tibetan Plateau. These patterns resemble the characteristics of an enhanced TEJ (Figure S9). The enhancement is likely a result of the La Niña like conditions (Figure 6a) and the associated Walker circulation response through

upper-level disturbances, as first described by (Shaman & Tziperman, 2007). Induced by La Niña, there is anomalous heating over the Tibetan Plateau (Duan *et al.*, 2012). The subsequent anomalous meridional temperature gradient leads to a strengthening of the TEJ core position over the Indian Ocean (Figure 6a; also Nithya *et al.*, 2017). Further evidence is provided by the spatial correlation patterns obtained by correlating the 200-hPa zonal wind, 200-hPa meridional wind, and 500-hPa vertical velocity, respectively, with the lagged synchronous index (see Equation 1). The correlation pattern resembles the structure of the tropical easterly jet (Nicholson & Klotter, 2021) (see also Supporting Information Figure S9 and compare with Figure S10). The pattern of an enhanced TEJ is not equally pronounced for the weak synchronization cluster (Figure 6e). Here, the zonal winds are only moderately enhanced over the equatorial Indian Ocean. In dry years, the zonal wind field is not enhanced over the Indian Ocean and the Bay of Bengal (Figure 6f). On the contrary, the pattern resembles a weakened TEJ (Figure S9b), which can be explained by the El Niño like SST pattern (Figure 6c).

3.3.4 | Enhanced moisture transport from the Arabian Sea

Further, during the MSDs for both clusters, we observe an increased inflow of moist air from the Arabian Sea via the cross-equatorial Somali Jet (Figure 6g,h). The Somali Jet is a major source of moisture during the ISM (Rai *et al.*, 2018). It is therefore consistent that the synchronization pattern is established mainly during the core monsoon season (Figure 3c) when the Somali Jet is most active. Further evidence is provided by the cold SST pattern observed in the Arabian Sean (Figure 6a,b), which is associated with increased evaporation and upwelling under the wind stress forcing due to a strengthened Somali jet. When this moisture flux hits the western Himalayan mountains, it leads to forced deep convection (Figure 5a,b,d). The anomalously strong convection in North India is thus—at least partially—forced by the anomalously strong moisture flux towards the orography. For dry years (Figure 3c), the synchronization is less pronounced and the enhanced Somali Jet inflow vanishes (Figure 6i), indicating that the moisture flux from the Arabian Sea is crucial for the initiation of synchronization.

3.3.5 | Combination of processes initiating the synchronization

Taken together, the initiation of the synchronization mechanism can be attributed to a threefold process.

Firstly, a negative PDO phase favors La Niña conditions (Figure 6a), promoting deep convection over peninsular India, facilitated by the anomalous Walker circulation response (Figure 5b). Secondly, this response supports the progression of the BSISO towards northwest India (Figure 5a), substantially enhancing the frequency of deep convection there. Thirdly, La Niña like conditions enhance the TEJ over India, but also over the Sahel (Figure 6d, Supporting Information Figure S10). We can provide strong statistical evidence for the importance of these three factors coming together. By estimating conditional probabilities (Equation 3) for the occurrence of MSDs, conditioned on the three potential impacting factors BSISO, ENSO, and the TEJ, we observe that the conditional probabilities for a day in JJAS being a MSD can be enhanced substantially compared with the respective null model. As expected from the analysis above, we find the most substantial increase for MSD for the conditioning on La Niña, an enhanced TEJ, as well as an active BSISO for phases 6, 7, and 8 (Figure 7e). In general, we find that an enhanced TEJ seems to be a necessary condition for synchronization to occur, as the likelihood of MSDs is increased when the TEJ is also enhanced (Figure 7a,c,e) for El Niño or neutral conditions. For a reduced TEJ, we observe hardly any synchronizations, even if the BSISO is active and La Niña conditions are present (Figure 7b,d,f), emphasizing the necessary role the TEJ plays in the occurrence of the synchronization pattern.

The combination of these three factors also becomes evident in a visual comparison. The pattern of anomalously negative OLR in Figure 5a occurs further north than on average for BSISO phases 6 and 7. However, when compositing the time points that are in the intersection of time points of La Niña years, have an enhanced TEJ, and are in BSISO phases 6 and 7 (Figure S16), the composited map resembles the composited MSD map (Figure 5a). The enhanced BSISO pushes moisture further north and northwest towards Pakistan. In this region, the dry static stability is very low, and anomalous moisture readily triggers convection. In consequence, we observe a significantly increased moistening of the middle to upper atmosphere from 500 to 200 hPa (Figure 5b).

3.4 | Mechanism driving synchronization between India and the Sahel

For the days before the synchronization is initiated, the OLR anomaly pattern shows a clear meridional dipole pattern between the Indian Ocean and the Indian mainland (Figure 8a) that is reminiscent of a classic BSISO-like structure (Kikuchi, 2021). We further observe a higher wave activity in the equatorial region during years with a strong
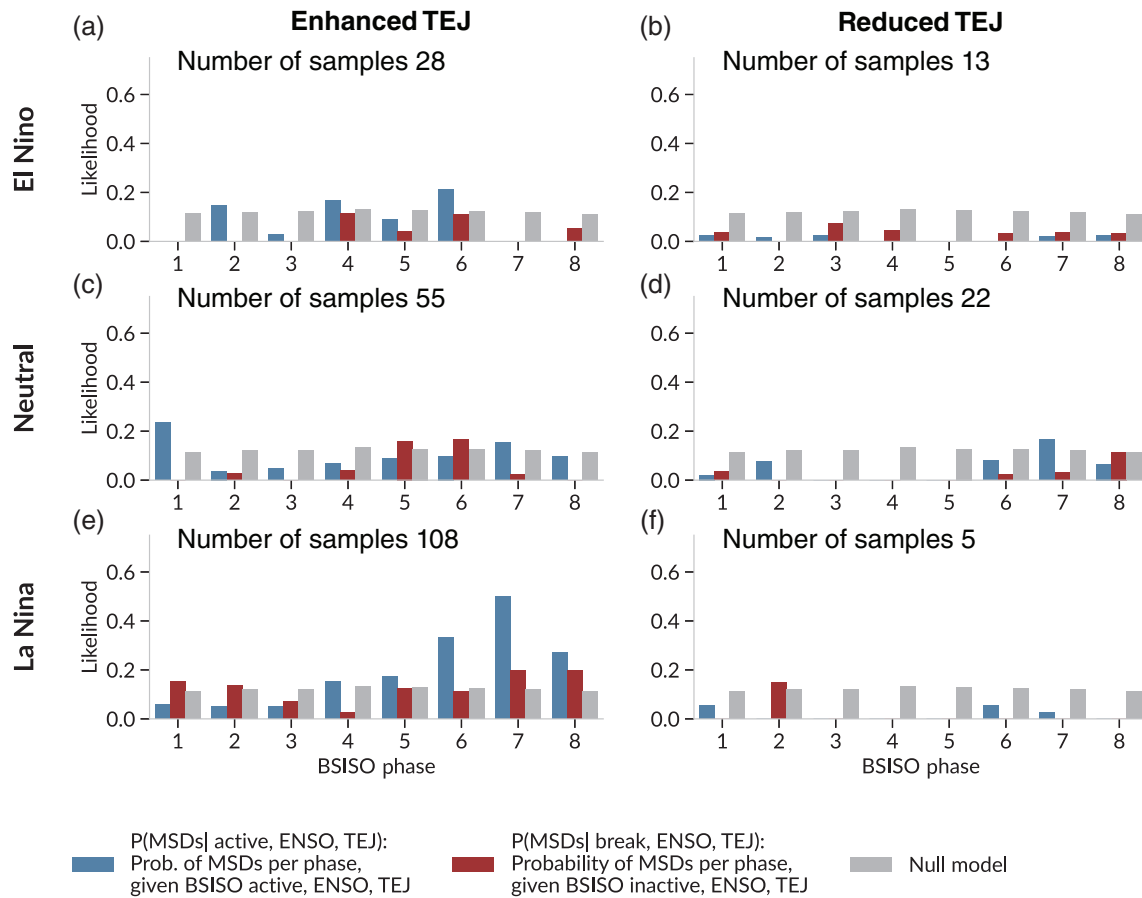
FIGURE 7 Probabilities for the occurrence of synchronization conditioned on BSISO phases, ENSO, and TEJ. (a–f) Most synchronous days (MSDs) are defined using the 90th percentile of the lagged synchronous index (see Section 2.5d). Their probability of occurrence is conditioned on the state of the Boreal Summer Intraseasonal Oscillation (BSISO), the Tropical Easterly Jet (TEJ), and the respective phase of the El Niño–Southern Oscillation (ENSO) for the respective time points computed as in Equation (3) (see Section 2.5). Blue (red) bars indicate an active (inactive) BSISO state conditioned on the state of ENSO and the TEJ. Gray bars denote the respective null model, that is, MSDs are assigned randomly to days in the JJAS season and assigned to the distribution of BSISO phases. [Colour figure can be viewed at wileyonlinelibrary.com]

synchronization pattern compared with years with less synchronization (years selected as shown in Figure 3c). We estimate the equatorial wave activity by Wheeler–Kiladis wavenumber-frequency spectrum plots ((Wheeler & Kiladis, 1999); Supporting Information Figure S6). In Figure 4, we see a slow westward propagation of negative OLR anomalies starting from the Arabian Sea and the northwest of India towards the Sahel. The westward-propagating OLR anomalies in the strong synchronization cluster resemble the westward propagation pattern in (Matthews, 2004; Janicot et al., 2009, 2011), which the authors call the "African MJO mode" (Janicot et al., 2011). Our composites in Figure 5d show that the strong convection in the northwest of India induces a meridional overturning circulation cell with the downward branch at around 10–15°N, which could be linked to the work of Ventrice et al. (2011), and Alaka & Maloney (2012), who suggest that the MJO in the equatorial

warm pool triggers convection initially around the Lake Chad Basin and the Ethiopian Highlands (around 20°E–30°E), though the process itself is not yet fully understood. In any case, we observe this convection happening in the OLR anomalies starting from day 0 to day +4 (Figure 4a,c) and to a lesser degree for the weak synchronization cluster a bit later at around day 4–8 (Figure 4d,f).

This region at around 20°E–30°E has been reported as a "trigger region" for AEW activity influenced by the AEJ (Leroux et al., 2010; Alaka & Maloney, 2012). We try to identify AEWs by using Hovmöller diagrams of the meridional wind overlaid with OLR anomalies. As single AEWs differ in their characteristics, that is, where valleys and peaks in the wave are, composite anomalies are not suited to visualizing the activity of AEWs over the Sahel. Instead, we have to study case-by-case events (see Figure S5 for some selected representative examples, similarly to Leroux et al. (2010)). Figure 8b shows one illustrative
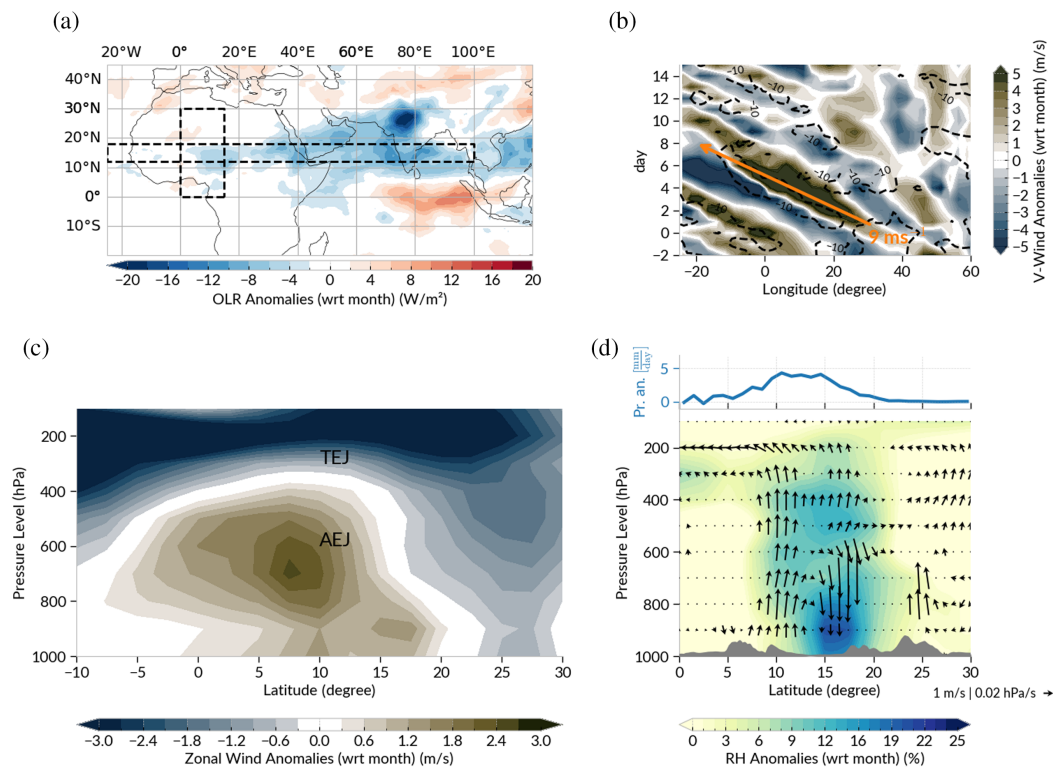
FIGURE 8 Conditions enabling synchronized ERE occurrences over the Sahel. (a) The background conditions for day −10 before the synchronization is initiated are shown. OLR anomalies visualize convective activity. The two rectangles denote the regions for the Hovmöller diagrams (in b) and the vertical cross-section plots (in c,d). (b) Hovmöller diagrams of the meridional V wind at 600 hPa for the zonal range [25°W, 100°E] overlaid with OLR anomalies (dashed contours) averaged over the region 10°N–18°N for one exemplary date included in the strong synchronization cluster. The orange arrow indicates the westward propagation direction of the wave and its estimated phase speed. (c) The vertical cross-section of the zonal wind anomalies averaged over 0°E–15°E for day 0. The region of the TEJ and the AEJ are indicated by text. The zonal wind anomalies are shown in m· s^{-1}. (d) The meridional circulation, averaged over 0°E–15°E for day +12. The top panel shows the zonally averaged precipitation anomalies (with respect to the month). The bottom panel shows the vertical structure of the circulation with arrows and the filled contours show relative humidity anomalies (computed with respect to the month). Gray contours visualize the orography. The wind fields are estimated using the zonally averaged V anomalies, measured in m· s^{-1}, and the vertical velocity ω in the horizontal direction, measured in pa· s^{-1}. Only statistically significant wind arrows at 95% confidence level using a two-sided t-test are shown. [Colour figure can be viewed at wileyonlinelibrary.com]

example of the zonal Hovmöller diagrams of V-wind anomalies at 600 hPa for one representative event, drawn from the strong synchronization cluster. In almost all single composites, we find a clear westward-propagating wave pattern that is accompanied by a westward-traveling OLR anomaly pattern. The speed of the wave can be estimated to be around 9 m · s^{-1}, which is consistent with the speed of AEWs as reported in (Thorncroft & Hoskins, 1994; Kiladis *et al.*, 2006), and most AEWs are initiated around the trigger region of 20°E–30°E. This analysis shows that the AEWs are indeed active during synchronization events.

AEWs are known to be bounded between the region of the AEJ and the TEJ (Lemburg *et al.*, 2019; Nicholson & Klotter, 2021) at around 600 hPa and increased AEW activity is linked to stronger vertical shear between the AEJ and the TEJ (Nicholson *et al.*, 2008). We find this pattern for the

strong synchronization cluster: the TEJ at around 200 hPa is enhanced and the AEJ at around 600 hPa is reduced (Figure 8c), resulting in an increased vertical shear of the zonal winds. Our analysis uncovers a propagation pattern of AEWs starting over the region where the convection occurs initially. This process induces rainfall by initiating mesoscale convective systems. This is shown by meridional cross-sections of the composite relative humidity anomalies on day +12 (Figure 8d). We find an overturning circulation, where convection occurs slightly off the Equator at around 10°N and is extremely deep, extending to the tropopause. The rising air coincides with the meridional core position of the reduced AEJ at 10°N (Figure 8c). This circulation overturns and leads to subsidence at both 5°N and 20°N. The anomalous increase of moisture content brought to the mid and upper troposphere leads to deep instability in a

region already characterized by widespread convection during this time of year, consistent with (Vizy & Cook, 2022). The anomalous deep convection moistens the mid-troposphere, reducing subsequent dry entrainment and ultimately leading to heavier widespread precipitation over the Sahel (Figure 8d).

Through the propagation of the westwards traveling AEWs, anomalous convection is then induced further westward towards the Western Coast as well. We can observe this in zonal cross-section plots of the U-wind anomalies (Figure S17). There is also a positive feedback, with the overturning circulation facilitating convergence in the lower levels, leading to the observed increase in near-surface humidity. In particular, we observe enhanced IVT inflow driven by the increased convective activity (Figure S13), which brings additional moisture from the Atlantic Ocean into the continent at levels around 800 hPa (Figure S17d–f). This also explains the observed increase in anomalous precipitation closer to the Atlantic coast (Supporting Information Figure 8c).

The rainfall extends over the full meridional range of the Sahel from 5°N–15°N. In the zonal direction, there are two peaks in intensity: one is over the Ethiopian Highlands, the other over the Northwest African coast. The former is likely due to orographic forcing at the Simien mountains, while the latter is a result of the moisture influx from the Atlantic Ocean (Figure 6g).

Composites of strong synchronization cluster days show only marginally enhanced intensity in the region of the upper-level TEJ at 200 hPa (compare the zonal circulation at day 0, Figure S17b, with that at day +12, Figure S17f). The upper-level easterlies do not differ substantially from the climatology, consistent with (Lemburg et al., 2019). Instead, anomalous convection happens from near the surface at 850 hPa up to about 400 hPa (Figure S17a–f). Hence, it is not the local variability of the TEJ on weekly to subseasonal time-scales that modulates the Sahel rainfall, but rather its variability on interannual time-scales. The strength of the teleconnection, therefore, also depends not on the local strength but on the positioning of the TEJ.

4 | DISCUSSION

We have identified and explained a teleconnection pattern linking extreme rainfall events (EREs) on a continental scale between the monsoons of North India. We first demonstrated that the synchronization pattern of EREs between North India and the Sahel Zone is a robust feature of the boreal summer monsoon system. The synchronization pattern is not a statistical artifact but rather is driven by anomalous large-scale atmospheric circulation, supported by the background state of the climate system. Our work thus provides a physical causal explanation for the teleconnection between the Asian and West African Monsoon domains.

We find that the synchronization is initiated by anomalously strong convection in the northwest of India, which is associated with an enhanced active phase of the BSISO. During La Niña conditions, there is typically a stronger South Asian monsoon (via the Walker circulation) and, driven by the BSISO, it is more likely for EREs to arise in northwest India (Strnad et al., 2023). The dynamics of the BSISO are central to the initiation of the synchronization pattern. Active phases of the BSISO also trigger the initiation of AEWs over the Sahel, which are enhanced further by the presence of reduced strength of the AEJ and increased strength of the TEJ, which is itself modulated by the La Niña conditions. The AEWs trigger convection, leading to a lagged occurrence of EREs over the Sahel Zone compared with over North India. Hence, the strength of this teleconnection depends on the positioning and amplitude of the TEJ and the periodicity of the BSISO.

While prior investigations have provided detailed insights into intraseasonal precipitation variability at a regional level in North India (Malik et al., 2010; Stolbova et al., 2014; Boers et al., 2019; Hunt et al., 2021; Hunt & Turner, 2022) and parts of the Sahel (Gleixner et al., 2017; Lemburg et al., 2019; Vashisht et al., 2021), our study integrates and consolidates these findings into a broader context. This synthesis enhances our comprehension of the underlying physical mechanisms, thereby holding the potential to enhance seasonal and subseasonal forecasts using windows of opportunities (Mariotti et al., 2020) during boreal summer in the tropical monsoon domain.

Still, some open questions remain. Firstly, the westward propagation over the Sahel shown in this study was uncovered by using OLR as a proxy for induced convection and consequently for intense rainfall. OLR has the advantage of being directly measurable and is therefore a reliable variable. However, it is not a direct measure of precipitation. Secondly, deep convective precipitation over the SZ relies on the interaction of several complex processes, including interactions of mesoscale convective systems with the East African Jet at around 600 hPa and the TEJ. Their interplay needs some further more local analysis. In particular, the mechanistic link between convection over northwest India and the Ethiopian highlands needs to be better understood. Thirdly, the role of the Circumglobal Teleconnection (CGT: (Ding & Wang, 2005)) in the synchronization between North India and the Sahel Zone is not fully understood. We find some patterns indicating a partial modulation by the CGT, but its effect seems to be minor. Further, future research could investigate the weak synchronization propagation cluster better. As the

previous analysis suggests that strong synchronization is the dominant process, the weak synchronization could be a combination of multiple and presumably more local interactions.

There are multiple ways to extend this work. One first step would be to test the occurrence of the synchronization pattern in current general circulation models (GCMs). On the one hand, an analysis of the teleconnection pattern in GCMs could provide insights into the robustness of the synchronization pattern. On the other hand, as precipitation dynamics and teleconnections are not always well reproduced in current GCMs (Boyle & Klein, 2010; Hess *et al.*, 2022; Douville *et al.*, 2023), the comparison could help to identify potential biases in the models. Our results provided a clear link between the BSISO, AEW activity, and the associated westward-propagating convection with associated increased likelihood of EREs. It would be interesting to investigate the potential link between the synchronization initiating AEWs and the genesis of tropical Atlantic cyclones (Thorncroft & Hodges, 2001; Russell *et al.*, 2017; Bercos-Hickey & Patricola, 2024). For example, (Ventrice *et al.*, 2011) showed that westward-propagating convection is linked to the genesis of tropical cyclones. Further, there are some studies emphasizing the role of AEWs in the genesis of North Atlantic hurricanes (Chen *et al.*, 2008). This could provide a new perspective on the global impact of the Indian monsoon system and its reported teleconnections to the North American west coast (Boers *et al.*, 2019).

Another next step could be to integrate knowledge about the uncovered teleconnection in current operational forecast systems. Of particular interest will be the representation of these synchronizations in deep learning global forecasts (for example Lam *et al.*, 2023; Bi *et al.*, 2023; Lessig *et al.*, 2023), which are more capable of capturing complex nonlinear relationships in the data.

CONFLICTS OF INTEREST
The authors declare that they have no competing interests.

DATA AVAILABILITY STATEMENT
Precipitation data were taken from the MSWEP dataset (https://www.gloh2o.org/mswep). Datasets for the composite analysis from 1979 until the current date were taken from Copernicus Climate Change Service (C3S) (https://cds.climate.copernicus.eu/cdsapp#!/dataset/reanalysis-era5-pressure-levels?tab=overview) (Hersbach et al., 2018).

The code for generating and analyzing the networks has been made publicly available by Strnad & Schlör (2023). The analysis uses the geoutils package (Strnad, 2023). The code for reproducing the analysis of the network communities and the data analysis in this article is publicly available at Strnad (2024). Plots were generated using the Cartopy (Met Office, 2010–2015) and Metpy v1.6 libraries (May *et al.*, 2022).

ENDNOTES
[1] https://psl.noaa.gov/enso/mei/ (last accessed April 10, 2024).
[2] https://www.data.gov.in/catalog/rainfall-india (last accessed: August 29, 2024).

ORCID
Felix M. Strnad https://orcid.org/0000-0001-6395-8150
Kieran M.R. Hunt https://orcid.org/0000-0003-1480-3755

REFERENCES
Alaka, G.J. & Maloney, E.D. (2012) The influence of the MJO on upstream precursors to African easterly waves. *Journal of Climate*, 25, 3219–3236.

Annamalai, H. & Slingo, J.M. (2001) Active/break cycles: diagnosis of the intraseasonal variability of the Asian summer monsoon. *Climate Dynamics*, 18, 85–102.

Bader, J. & Latif, M. (2003) The impact of decadal-scale Indian Ocean sea surface temperature anomalies on Sahelian rainfall and the North Atlantic oscillation. *Geophysical Research Letters*, 30.

Beck, H.E., Pan, M., Roy, T., Weedon, G.P., Pappenberger, F., van Dijk, A.I.J.M. *et al.* (2019a) Daily evaluation of 26 precipitation datasets using stage-IV gauge-radar data for the CONUS. *Hydrology and Earth System Sciences*, 23, 207–224.

Beck, H.E., Wood, E.F., Pan, M., Fisher, C.K., Miralles, D.G., van Dijk, A.I.J.M. *et al.* (2019b) MSWEP V2 global 3-hourly 0.1 precipitation: methodology and quantitative assessment. *Bulletin of the American Meteorological Society*, 100, 473–500.

Bendito, E., Carmona, A., Encinas, A.M. & Gesto, J.M. (2007) Estimation of Fekete points. *Journal of Computational Physics*, 225, 2354–2376.

Bercos-Hickey, E. & Patricola, C.M. (2024) Characteristics and trends of Atlantic tropical cyclones that do and do not develop from African easterly waves. *Quarterly Journal of the Royal Meteorological Society*, 150(765), 4951–4968.

Beverley, J.D., Woolnough, S.J., Baker, L.H., Johnson, S.J. & Weisheimer, A. (2019) The northern hemisphere circumglobal teleconnection in a seasonal forecast model and its relationship to European summer forecast skill. *Climate Dynamics*, 52, 3759–3771.

Beverley, J.D., Woolnough, S.J., Baker, L.H., Johnson, S.J., Weisheimer, A. & O'Reilly, C.H. (2021) Dynamical mechanisms linking Indian monsoon precipitation and the circumglobal teleconnection. *Climate Dynamics*, 57, 2615–2636.

Bi, K., Xie, L., Zhang, H., Chen, X., Gu, X. & Tian, Q. (2023) Accurate medium-range global weather forecasting with 3D neural networks. *Nature*, 619, 533–538.

Bickle, M.E., Marsham, J.H., Ross, A.N., Rowell, D.P., Parker, D.J. & Taylor, C.M. (2021) Understanding mechanisms for trends in Sahelian squall lines: roles of thermodynamics and shear. *Quarterly Journal of the Royal Meteorological Society*, 147, 983–1006.

Bishop, C.M. & Nasrabadi, N.M. (2006) *Pattern recognition and machine learning*, Vol. 4. New York, NY: Springer.

Boers, N., Bookhagen, B., Barbosa, H.M.J., Marwan, N., Kurths, J. & Marengo, J.A. (2014) Prediction of extreme floods in the eastern Central Andes based on a complex networks approach. *Nature Communications*, 5, 1–7.

Boers, N., Goswami, B., Rheinwalt, A., Bookhagen, B., Hoskins, B. & Kurths, J. (2019) Complex networks reveal global pattern of extreme-rainfall teleconnections. *Nature*, 566, 373–377. URL: Available from: http://www.nature.com/articles/s41586-018-0872-x

Bordoni, S. & Schneider, T. (2008) Monsoons as eddy-mediated regime transitions of the tropical overturning circulation. *Nature Geoscience*, 1, 515–519.

Boyle, J. & Klein, S.A. (2010) Impact of horizontal resolution on climate model forecasts of tropical precipitation and diabatic heating for the TWP-ICE period. *Journal of Geophysical Research – Atmospheres*, 115.

Chang, C.-H., Johnson, N.C. & Yoo, C. (2021) Evaluation of sub-seasonal impacts of the MJO/BSISO in the east Asian extended summer. *Climate Dynamics*, 56, 3553–3568.

Chen, T. & van Loon, H. (1987) Interannual variation of the tropical easterly jet. *Monthly Weather Review*, 115, 1739–1759.

Chen, T.-C., Wang, S.-Y. & Clark, A.J. (2008) North Atlantic hurricanes contributed by African easterly waves north and south of the African easterly jet. *Journal of Climate*, 21, 6767–6776.

Cherchi, A. & Navarra, A. (2013) Influence of ENSO and of the Indian Ocean dipole on the Indian summer monsoon variability. *Climate Dynamics*, 41, 81–103.

Di Lorenzo, E., Xu, T., Zhao, Y., Newman, M., Capotondi, A., Stevenson, S. *et al.* (2023) Modes and mechanisms of Pacific decadal-scale variability. *Annual Review of Marine Science*, 15, 249–275.

Ding, Q. & Wang, B. (2005) Circumglobal teleconnection in the northern hemisphere summer. *Journal of Climate*, 18, 3483–3505.

Ding, Q. & Wang, B. (2007) Intraseasonal teleconnection between the summer Eurasian wave train and the Indian monsoon. *Journal of Climate*, 20, 3751–3767.

Douville, H., Raghavan, K., Renwick, J., Allan, R., Arias, P., Barlow, M. et al. (2023) *Water cycle Changes*. Cambridge: Cambridge University Press, pp. 1055–1210.

Duan, A., Wu, G., Liu, Y., Ma, Y. & Zhao, P. (2012) Weather and climate effects of the Tibetan plateau. *Advances in Atmospheric Sciences*, 29, 978–992.

Fan, F., Dong, X., Fang, X., Xue, F., Zheng, F. & Zhu, J. (2017) Revisiting the relationship between the south Asian summer monsoon drought and El Niño warming pattern. *Atmospheric Science Letters*, 18, 175–182.

Folland, C.K., Palmer, T.N. & Parker, D.E. (1986) Sahel rainfall and worldwide sea temperatures, 1901–85. *Nature*, 320, 602–607.

Geen, R., Bordoni, S., Battisti, D.S. & Hui, K. (2020) Monsoons, ITCZs, and the concept of the global monsoon. *Reviews of Geophysics*, 58, e2020RG000700.

Gleixner, S., Keenlyside, N., Viste, E. & Korecha, D. (2017) The El Niño effect on Ethiopian summer rainfall. *Climate Dynamics*, 49, 1865–1883.

Grist, J.P. & Nicholson, S.E. (2001) A study of the dynamic factors influencing the rainfall variability in the west African Sahel. *Journal of Climate*, 14, 1337–1359.

Gupta, S., Su, Z., Boers, N., Kurths, J., Marwan, N. & Pappenberger, F. (2022) Interconnection between the Indian and the east Asian summer monsoon: spatial synchronization patterns of extreme rainfall events. *International Journal of Climatology*, 43(2), 1034–1049.

Hall, N.M.J. & Peyrillé, P. (2006) Dynamics of the west African monsoon. *Journal de Physique IV France*, 139, 81–99.

Hamilton, H.L., Ocasio, K.M.N., Evans, J.L., Young, G.S. & Fuentes, J.D. (2020) Topographic influence on the African easterly jet and African easterly wave energetics. *Journal of Geophysical Research – Atmospheres*, 125, e2019JD032138.

Hersbach, H., Bell, B., Berrisford, P., Biavati, G., Horányi, A., Muñoz Sabater, J. et al. (2018) Era5 Hourly Data on Single Levels From 1979 to Present. Accessed on March 02, 2022.

Hersbach, H., Bell, B., Berrisford, P., Hirahara, S., Horányi, A., Muñoz-Sabater, J. et al. (2020) The ERA5 global reanalysis. *Quarterly Journal of the Royal Meteorological Society*, 146, 1999–2049.

Hess, P., Drüke, M., Petri, S., Strnad, F.M. & Boers, N. (2022) Physically constrained generative adversarial networks for improving precipitation fields from earth system models. *Nature Machine Intelligence*, 4, 828–839.

Huang, S., Wang, B., Wen, Z. & Chen, Z. (2021) Enhanced tropical eastern Indian Ocean rainfall breaks down the tropical easterly jet–Indian rainfall relationship. *Journal of Climate*, 34, 3039–3048.

Huang, S., Wen, Z., Chen, Z., Li, X., Chen, R. & Guo, Y. (2019) Interdecadal change in the relationship between the tropical easterly jet and tropical sea surface temperature anomalies in boreal summer. *Climate Dynamics*, 53, 2119–2131.

Hunt, K.M.R. & Turner, A.G. (2022) Nonlinear intensification of monsoon low pressure systems by the BSISO. *Weather and Climate Dynamics*, 3(4), 1341–1358. URL: Available from: https://doi.org/10.5194/wcd-3-1341-2022

Hunt, K.M.R., Turner, A.G. & Schiemann, R.K.H. (2021) How interactions between tropical depressions and Western disturbances affect heavy precipitation in South Asia. *Monthly Weather Review*, 149, 1801–1825.

Janicot, S., Caniaux, G., Chauvin, F., de Coëtlogon, G., Fontaine, B., Hall, N. et al. (2011) Intraseasonal variability of the west African monsoon. *Atmospheric Science Letters*, 12, 58–66.

Janicot, S., Mounier, F., Hall, N.M.J., Leroux, S., Sultan, B. & Kiladis, G.N. (2009) Dynamics of the west African monsoon. Part IV: analysis of 25–90-day variability of convection and the role of the Indian monsoon. *Journal of Climate*, 22, 1541–1565.

Jiang, X., Li, T. & Wang, B. (2004) Structures and mechanisms of the northward propagating boreal summer Intraseasonal oscillation. *Journal of Climate*, 17, 1022–1039.

Joh, Y., Delworth, T.L., Wittenberg, A.T., Yang, X., Rosati, A., Johnson, N.C. et al. (2023) The role of upper-ocean variations of the Kuroshio-Oyashio extension in seasonal-to-decadal air-sea heat flux variability. *Npj Clim. Atmospheric Sciences*, 6, 1–11.

Joly, M., Voldoire, A., Douville, H., Terray, P. & Royer, J.-F. (2007) African monsoon teleconnections with tropical SSTs: validation and evolution in a set of IPCC4 simulations. *Climate Dynamics*, 29, 1–20.

Kikuchi, K. (2021) The boreal summer Intraseasonal oscillation (BSISO): a review. *Journal of the Meteorological Society of Japan. Ser. II*, 99, 2021–2045.

Kikuchi, K., Wang, B. & Kajikawa, Y. (2012) Bimodal representation of the tropical intraseasonal oscillation. *Climate Dynamics*, 38, 1989–2000.

Kiladis, G.N., Dias, J., Straub, K.H., Wheeler, M.C., Tulich, S.N., Kikuchi, K. et al. (2014) A comparison of OLR and circulation-based indices for tracking the MJO. *Monthly Weather Review*, 142, 1697–1715.

Kiladis, G.N., Thorncroft, C.D. & Hall, N.M.J. (2006) Three-dimensional structure and dynamics of African easterly waves. *Part I: Observations. J. Atmos. Sci.*, 63, 2212–2230.

Koteswaram, P. (1958) The easterly jet stream in the tropics. *Tellus*, 10(1), 43–57. URL: Available from: https://www.tandfonline.com/doi/abs/10.3402/tellusa.v10i1.9220

Kotz, M., Levermann, A. & Wenz, L. (2022) The effect of rainfall changes on economic production. *Nature*, 601, 223–227.

Kumar, K.K., Rajagopalan, B., Hoerling, M., Bates, G. & Cane, M. (2006) Unraveling the mystery of Indian monsoon failure during El Niño. *Science*, 314, 115–119.

Lam, R., Sanchez-Gonzalez, A., Willson, M., Wirnsberger, P., Fortunato, M., Alet, F. et al. (2023) Learning skillful medium-range global weather forecasting. *Science*, 382, 1416–1421.

Lee, J.-Y., Wang, B., Wheeler, M.C., Fu, X., Waliser, D.E. & Kang, I.-S. (2013) Real-time multivariate indices for the boreal summer intraseasonal oscillation over the Asian summer monsoon region. *Climate Dynamics*, 40, 493–509.

Lemburg, A., Bader, J. & Claussen, M. (2019) Sahel rainfall–tropical easterly jet relationship on synoptic to Intraseasonal time scales. *Monthly Weather Review*, 147, 1733–1752.

Leroux, S., Hall, N.M.J. & Kiladis, G.N. (2010) A climatological study of transient–mean-flow interactions over West Africa. *Quarterly Journal of the Royal Meteorological Society*, 136, 397–410.

Lessig, C., Luise, I., Gong, B., Langguth, M., Stadtler, S. & Schultz, M. (2023) AtmoRep: a stochastic model of atmosphere dynamics using large scale representation learning. *arXiv*.

Madden, R.A. & Julian, P.R. (1971) Detection of a 40–50 day oscillation in the zonal wind in the tropical Pacific. *Journal of the Atmospheric Sciences*, 28, 702–708.

Madhu, V. (2014) Variation of zonal winds in the upper troposphere and lower stratosphere in association with deficient and excess Indian summer monsoon scenario. *Atmospheric and Climate Sciences*, 4, 685–695.

Malik, N., Marwan, N. & Kurths, J. (2010) Spatial structures and directionalities in monsoonal precipitation over South Asia. *Nonlinear Processes in Geophysics*, 17, 371–381.

Maloney, E.D. & Shaman, J. (2008) Intraseasonal variability of the west African monsoon and Atlantic ITCZ. *Journal of Climate*, 21, 2898–2918.

Mariotti, A., Baggett, C., Barnes, E.A., Becker, E., Butler, A., Collins, D.C. et al. (2020) Windows of opportunity for Skillful forecasts subseasonal to seasonal and beyond. *Bulletin of the American Meteorological Society*, 101, E608–E625.

Matthews, A.J. (2004) Intraseasonal variability over tropical africa during northern summer. *Journal of Climate*, 17, 2427–2440.

May, R.M., Goebbert, K.H., Thielen, J.E., Leeman, J.R., Camron, M.D., Bruick, Z. et al. (2022) Metpy: a meteorological python library for data analysis and visualization. *Bulletin of the American Meteorological Society*, 103, E2273–E2284. URL: Available from: https://journals.ametsoc.org/view/journals/bams/103/10/BAMS-D-21-0125.1.xml

Office, M. (2010–2015) Cartopy: a cartographic python library with a Matplotlib interface. *Exeter, Devon*. URL: Available from: http://scitools.org.uk/cartopy

Meyers, G., McIntosh, P., Pigot, L. & Pook, M. (2007) The years of El Niño, La Niña, and interactions with the tropical Indian Ocean. *Journal of Climate*, 20, 2872–2880.

Mohino, E., Janicot, S., Douville, H. & Li, L.Z.X. (2012) Impact of the Indian part of the summer MJO on West Africa using nudged climate simulations. *Climate Dynamics*, 38, 2319–2334.

Niang, C., Mohino, E., Gaye, A.T. & Omotosho, J.B. (2017) Impact of the Madden Julian oscillation on the summer west African monsoon in AMIP simulations. *Climate Dynamics*, 48, 2297–2314.

Nicholson, S.E. (2008) The intensity, location and structure of the tropical rainbelt over west Africa as factors in interannual variability. *International Journal of Climatology*, 28, 1775–1785.

Nicholson, S.E. (2013) The west African Sahel: a review of recent studies on the rainfall regime and its interannual variability. *Intl. Scholarly Res. Notices*, 2013, 453521.

Nicholson, S.E., Barcilon, A.I. & Challa, M. (2008) An analysis of west African dynamics using a linearized GCM. *Journal of the Atmospheric Sciences*, 65, 1182–1203.

Nicholson, S.E. & Klotter, D. (2021) The tropical easterly jet over Africa, its representation in six reanalysis products, and its association with Sahel rainfall. *International Journal of Climatology*, 41, 328–347.

Nikumbh, A.C., Chakraborty, A., Bhat, G.S. & Frierson, D.M.W. (2021) Multiscale interactions between monsoon Intraseasonal oscillations and low pressure systems that produce heavy rainfall events of different spatial extents. *Journal of Climate*, 34, 9523–9534.

Nikumbh, A.C., Thakur, A.B.S., Chakraborty, A., Bhat, G.S. & Sukhatme, J. (2023) The role of the North Atlantic blocking high during large-scale heavy rainfall events over Central India. *Journal of the Atmospheric Sciences*, 80, 1815–1827.

Nithya, K., Manoj, M.G. & Mohankumar, K. (2017) Effect of El Niño/La Niña on tropical easterly jet stream during Asian summer monsoon season. *International Journal of Climatology*, 37, 4994–5004.

Parthasarathy, B., Munot, A.A. & Kothawale, D.R. (1994) All-India monthly and seasonal rainfall series: 1871–1993. *Theoretical and Applied Climatology*, 49, 217–224.

Pattanaik, D.R. & Satyan, V. (2000) Fluctuations of tropical easterly jet during contrasting monsoons over India: a GCM study. *Meteorology and Atmospheric Physics*, 75, 51–60.

Peixoto, T.P. (2014a) The graph-tool python library. *Figshare*. URL: Available from: http://figshare.com/articles/graph.tool/1164194

Peixoto, T.P. (2014b) Hierarchical block structures and high-resolution model selection in large networks. *Physical Review X*, 4, 1–18.

Peixoto, T.P. (2019) Bayesian stochastic Blockmodeling. In: *Advances in network clustering and Blockmodeling*. Chichester, England, UK: John Wiley & Sons, Ltd, pp. 289–332.

Priya, P., Mujumdar, M., Sabin, T.P., Terray, P. & Krishnan, R. (2015) Impacts of indo-Pacific Sea surface temperature anomalies on the summer monsoon circulation and heavy precipitation over Northwest India–Pakistan region during 2010. *Journal of Climate*, 28, 3714–3730.

Quian Quiroga, R., Kreuz, T. & Grassberger, P. (2002) Event synchronization: a simple and fast method to measure synchronicity and time delay patterns. *Physical Review E*, 66, 041904.

Rai, P., Joshi, M., Dimri, A.P. & Turner, A.G. (2018) The role of potential vorticity anomalies in the Somali jet on Indian summer monsoon Intraseasonal variability. *Climate Dynamics*, 50, 4149–4169.

Rajeevan, M., Gadgil, S. & Bhate, J. (2010) Active and break spells of the Indian summer monsoon. *Journal of Earth System Science*, 119, 229–247.

Rao, S. & Srinivasan, J. (2016) The impact of latent heating on the location and strength of the tropical easterly jet. *Meteorology and Atmospheric Physics*, 128, 247–261.

Rousseeuw, P.J. (1987) Silhouettes: a graphical aid to the interpretation and validation of cluster analysis. *Journal of Computational and Applied Mathematics*, 20, 53–65.

Russell, J.O., Aiyyer, A., White, J.D. & Hannah, W. (2017) Revisiting the connection between African easterly waves and Atlantic tropical cyclogenesis. *Geophysical Research Letters*, 44, 587–595.

Sathiyamoorthy, V. (2005) Large scale reduction in the size of the tropical easterly jet. *Geophysical Research Letters*, 32.

Sathiyamoorthy, V., Pal, P.K. & Joshi, P.C. (2007) Intraseasonal variability of the tropical easterly jet. *Meteorology and Atmospheric Physics*, 96, 305–316.

Schlör, J., Strnad, F., Capotondi, A. & Goswami, B. (2024) Contribution of El Niño southern oscillation (ENSO) diversity to low-frequency changes in ENSO variance. *Geophysical Research Letters*, 51, e2024GL109179.

Schlueter, A., Fink, A.H., Knippertz, P. & Vogel, P. (2019) A systematic comparison of tropical waves over northern Africa. Part I: influence on rainfall. *Journal of Climate*, 32, 1501–1523.

Shaman, J. & Tziperman, E. (2007) Summertime ENSO–north African–Asian jet teleconnection and implications for the Indian monsoons. *Geophysical Research Letters*, 34.

Skinner, C.B. & Diffenbaugh, N.S. (2013) The contribution of African easterly waves to monsoon precipitation in the CMIP3 ensemble. *Journal of Geophysical Research – Atmospheres*, 118, 3590–3609.

Sooraj, K.P., Terray, P., Shilin, A. & Mujumdar, M. (2020) Dynamics of rainfall extremes over India: a new perspective. *International Journal of Climatology*, 40, 5223–5245.

Sossa, A., Liebmann, B., Bladé, I., Allured, D., Hendon, H.H., Peterson, P. et al. (2017) Statistical connection between the Madden–Julian oscillation and large daily precipitation events in West Africa. *Journal of Climate*, 30, 1999–2010.

Stolbova, V., Martin, P., Bookhagen, B., Marwan, N. & Kurths, J. (2014) Topology and seasonal evolution of the network of extreme precipitation over the Indian subcontinent and Sri Lanka. *Nonlinear Processes in Geophysics*, 21, 901–917.

Strnad, F. (2023) *Fstrnad/Geoutils: Geoutils*. Zenodo. URL. Available from: https://doi.org/10.5281/zenodo.8354788

Strnad, F. (2024) *Monsoon synchronization*. Zenodo. URL. Available from: https://github.com/fstrnad/monsoon.synchronization

Strnad, F. & Schlör, J. (2023) Climnet v.2.2.0.

Strnad, F.M., Schlör, J., Fröhlich, C. & Goswami, B. (2022) Teleconnection patterns of different El Niño types revealed by climate network curvature. *Geophysical Research Letters*, 49, e2022GL098571.

Strnad, F.M., Schlör, J., Geen, R., Boers, N. & Goswami, B. (2023) Propagation pathways of indo-Pacific rainfall extremes are modulated by Pacific sea surface temperatures. *Nature Communications*, 14, 1–16.

Thorncroft, C. & Hodges, K. (2001) African easterly wave variability and its relationship to Atlantic tropical cyclone activity. *Journal of Climate*, 14, 1166–1179.

Thorncroft, C.D., Hall, N.M. & Kiladis, G.N. (2008) Three-dimensional structure and dynamics of african easterly waves. Part III: genesis. *Journal of the Atmospheric Sciences*, 65, 3596–3607.

Thorncroft, C.D. & Hoskins, B.J. (1994) An idealized study of African easterly waves. I: a linear view. *Quarterly Journal of the Royal Meteorological Society*, 120, 953–982.

Tsonis, A.A. & Swanson, K.L. (2008) Topology and predictability of El Niño and La Niña networks. *Physical Review Letters*, 100, 228502.

Vashisht, A., Zaitchik, B. & Gnanadesikan, A. (2021) ENSO teleconnection to eastern African summer rainfall in global climate models: role of the tropical easterly jet. *Journal of Climate*, 34, 293–312.

Vellore, R.K., Krishnan, R., Pendharkar, J., Choudhury, A.D. & Sabin, T.P. (2014) On the anomalous precipitation enhancement over the Himalayan foothills during monsoon breaks. *Climate Dynamics*, 43, 2009–2031.

Ventrice, M.J., Thorncroft, C.D. & Roundy, P.E. (2011) The Madden–Julian Oscillation's influence on African easterly waves and downstream tropical cyclogenesis. *Monthly Weather Review*, 139, 2704–2722.

Vizy, E.K. & Cook, K.H. (2022) Distribution of extreme rainfall events and their environmental controls in the west African Sahel and Soudan. *Climate Dynamics*, 59, 997–1026.

Walker, J.M., Bordoni, S. & Schneider, T. (2015) Interannual variability in the large-scale dynamics of the south Asian summer monsoon. *Journal of Climate*, 28, 3731–3750.

Wang, B. & Ding, Q. (2008) Global monsoon: dominant mode of annual variation in the tropics. *Dynamics of Atmospheres and Oceans*, 44, 165–183.

Wang, S. & Sobel, A.H. (2022) A unified moisture mode theory for the Madden–Julian oscillation and the boreal summer Intraseasonal oscillation. *Journal of Climate*, 35, 1267–1291.

Webster, P. (2020) *Dynamics of the tropical atmosphere and oceans*. John Wiley & Sons, Ltd.

Wheeler, M. & Kiladis, G.N. (1999) Convectively coupled equatorial waves: analysis of clouds and temperature in the wavenumber–frequency domain. *Journal of the Atmospheric Sciences*, 56, 374–399.

Wheeler, M.C. & Hendon, H.H. (2004) An all-season real-time multivariate MJO index: development of an index for monitoring and prediction. *Monthly Weather Review*, 132, 1917–1932.

Whittleston, D., Nicholson, S.E., Schlosser, A. & Entekhabi, D. (2017) Climate models lack jet–rainfall coupling over West Africa. *Journal of Climate*, 30, 4625–4632.

Wolter, K. & Timlin, M.S. (2011) El Niño/southern oscillation behaviour since 1871 as diagnosed in an extended multivariate ENSO index (MEI.Ext). *International Journal of Climatology*, 31, 1074–1087.

Xavier, P.K., Marzin, C. & Goswami, B.N. (2007) An objective definition of the Indian summer monsoon season and a new perspective on the ENSO–monsoon relationship. *Quarterly Journal of the Royal Meteorological Society*, 133, 749–764.

Zhang, C. (2005) Madden-Julian oscillation. *Reviews of Geophysics*, 43.

Zhang, C., Adames, Á.F., Khouider, B., Wang, B. & Yang, D. (2020) Four theories of the Madden-Julian oscillation. *Reviews of Geophysics*, 58, e2019RG000685.

SUPPORTING INFORMATION

Additional supporting information can be found online in the Supporting Information section at the end of this article.